International Journal of Fatigue 215 (2027) 109957

Contents lists available at ScienceDirect

International Journal of Fatigue

journal homepage: www.elsevier.com/locate/ijfatigue

# A unified mechanics theory framework for fully reversed high cycle fatigue of FCC aluminum based on two-scale microplasticity entropy production

Hsiao Wei Lee

*Department of Aeronautics and Astronautics, National Cheng Kung University, Tainan, Taiwan, ROC*

ARTICLE INFO

*Keywords:*
Unified mechanics theory
Fatigue
Entropy
Plasticity
Dislocation

ABSTRACT

Unified Mechanics Theory (UMT) relates cumulative entropy production to material degradation through a thermodynamic state index (TSI) derived from Boltzmann's entropy formula. Although TSI evolution does not require an empirically fitted law, the entropy-generation formulation remains material- and loading-specific. Existing UMT high cycle fatigue (HCF) models, developed primarily for body-centered cubic steels, therefore require reformulation for face-centered cubic alloys. This study develops a UMT-based framework for conventional fully reversed HCF of FCC aluminum alloys. Localized cyclic irreversibility is represented by a two-scale microplastic region embedded in an elastic matrix. The defect-scale flow rule is reformulated using an Eyring-type relation without imposing an explicit fatigue threshold, and entropy production is calculated from cumulative microplastic dissipation. Using a literature-based parameter set, the predicted fatigue lives agree well with fully reversed HCF data for smooth cylindrical dog-bone specimens made of AA7075-T651 aluminum alloy and tested at 0.5–10 Hz over a range of stress amplitudes. Additional calculations at various stress ratios $R$ assess the model's numerical behavior and reveal rapid local shakedown associated with the present linear kinematic-hardening formulation. A secondary study of smooth flat dog-bone specimens uses a separate literature-based parameter set for the $R = -1$ baseline and subsequently retains it for prediction at $R \approx 0$ without further adjustment. The predictions reproduce the experimental S–N trend but moderately overpredict fatigue life at $R \approx 0$, highlighting a remaining limitation under tensile mean stress. Alternative microstructural parameter evolution laws and coupled-sensitivity studies further assess parameter uncertainty and interactions.

## 1. Introduction

Reliable fatigue-life prediction and cumulative-damage assessment are central to aerospace design because structural components and rotating machinery experience complex cyclic loading histories. Turbine blades and disks undergo low-cycle fatigue (LCF) during engine start-up and shutdown, when substantial local cyclic plastic deformation may develop [1,2]. They also experience high-frequency vibratory loading caused by fluctuations in the turbine-driving gas flow, which can induce high cycle fatigue (HCF) at stresses below the macroscopic yield strength. Cracks may then initiate from microscopic defects and propagate to catastrophic failure with little warning [2–4]. Aircraft fuselages and wing-root regions, commonly made from high-strength aluminum alloys, are likewise subjected to cabin-pressurization and ground–air–ground cycles, promoting damage at rivet holes, fastener sites, and joints [5–7]. Accordingly, both LCF and HCF degradation mechanisms must be considered in aerospace fatigue design and life assessment.

Conventionally, metallic fatigue life is predicted using strain-life relations for LCF, such as the Coffin–Manson relation [8–10], and stress-life relations for HCF, such as the Basquin equation [10,11], often combined with Palmgren–Miner's linear damage rule [12–15]. Although widely used, these approaches are empirical or semi-empirical because their coefficients are calibrated to experimental data. Continuum damage mechanics (CDM) models have also been extensively developed [16–18]. Despite their thermodynamically consistent constitutive basis, their degradation potentials and damage evolution laws are often phenomenological and still require empirical assumptions or calibration [10,19–21]. Consequently, both curve-fitted fatigue relations and phenomenological damage-evolution models may be case-dependent and unreliable when extrapolated across materials, frequencies, stress ratios, or environments. They may also struggle to represent different initial damage states or coupled degradation mechanisms, such as corrosion-fatigue [22–24] and hydrogen-assisted fatigue [25–27], which require specialized multiphysics treatment.

In recent years, cumulative thermodynamic entropy production has emerged as a physics-based measure for quantifying fatigue-damage

*E-mail address:* hwlee@gs.ncku.edu.tw.

https://doi.org/10.1016/j.ijfatigue.2026.109957
Received 9 May 2026; Received in revised form 7 August 2026; Accepted 26 August 2026
Available online 3 September 2026

accumulation and estimating remaining life [28–34]. Within this context, Unified Mechanics Theory (UMT) [35–37] relates material degradation to cumulative entropy production through a thermodynamic state index (TSI) derived from Boltzmann's interpretation of entropy and disorder. The same entropy-based TSI evolution law is applied across different irreversible degradation processes, thereby avoiding the need to postulate a separate process-specific scalar degradation law for each application. This universality, however, applies to the TSI evolution law rather than to the complete constitutive formulation within the model. Importantly, the entropy-generation equation remains material- and loading-specific and must represent the dominant irreversible mechanisms of the problem under consideration. Its formulation may therefore still involve physical idealizations, phenomenological or semi-empirical relations, and parameters obtained from experiments, literature, or calibration.

UMT has been applied under electrical [38], thermal [39,40], chemical [41], and mechanical loading conditions [42–47], including experimentally validated fatigue-life and degradation studies. However, existing UMT formulations for metallic HCF were developed primarily for BCC steels and are not directly transferable to FCC aluminum alloys, which are widely used in aerospace structures. The earlier formulation imposed an explicit microscopic fatigue threshold below which no microplasticity or associated entropy production was predicted. This assumption is more compatible with BCC steels, where the comparatively high Peierls barrier increases lattice resistance to dislocation motion and may contribute to an apparent endurance limit. In contrast, FCC aluminum alloys generally exhibit lower lattice resistance, lack a distinct endurance limit, and may retain finite cyclic microplasticity at low stress amplitudes. The earlier model also represented frequency effects through an external frequency-ratio coefficient and assumed an already stabilized defect-scale hysteresis loop, without explicitly resolving time-dependent kinetics or the transition from the initial response to stabilization. These limitations motivate the present FCC formulation with thermally activated flow, no explicitly imposed fatigue threshold, and an evolving defect-scale response.

The objective of the present work is to formulate and numerically evaluate a revised two-scale microplasticity model for computing localized dissipation and the associated entropy production, and to assess its performance against available experimental data. The study focuses on room-temperature, constant-amplitude, conventional HCF of AA7075-T651 under fully reversed loading ($R = -1$). The principal contributions are: (i) an Eyring-type microplasticity model for defect-scale slip without an explicit fatigue threshold; (ii) an explicitly derived, work-conjugate microplastic dissipation measure as the entropy source; (iii) an assessment of alternative bounded microstructural parameter evolution laws for the active micro-defect fraction and micro-kinematic hardening modulus; and (iv) a hierarchical cycle/block integration scheme for efficient computation of entropy accumulation over millions of loading cycles. The primary benchmark prediction uses smooth cylindrical dog-bone specimen data at $R = -1$, while a secondary study of smooth flat dog-bone specimens compares predictions at $R = -1$ and then evaluates performance at $R \approx 0$ without parameter recalibration. Additional simulations at specified stress ratios examine rapid local shakedown and discuss limitations of the present formulation. The model shows good agreement with the fully reversed data but overpredicts fatigue life at $R \approx 0$, indicating that further development is needed to account for tensile mean-stress effects. Explicit PSB evolution, grain-boundary cavities, manufacturing-defect geometry, probabilistic scatter, and variable-amplitude loading with history dependence remain beyond the scope of the present mean-field framework.

The intended advantage of the UMT-based fatigue model is that, once the relevant entropy-generation formulation and the required kinetic, microstructural, and mechanical parameters are established for a given material, fatigue response can be evaluated using the same TSI evolution law without introducing a separate empirical degradation law for each case. In the present study, however, calculations beyond the fully reversed condition are interpreted as assessments of numerical capability rather than validated transferability. Parameter sensitivity and interaction analyses, together with assessments of alternative laws governing microstructural parameter evolution, are used to quantify parameter effects and associated uncertainties.

## 2. Derivation of the entropy production model

To contextualize the proposed model, we first revisit the definition of the TSI within the UMT framework, then examine the entropy-generation mechanisms underlying high cycle fatigue (HCF) in metals, and finally adapt the microplasticity-based entropy production framework previously developed for BCC metals to FCC metals [41–43].

### 2.1. The thermodynamic state index

In Boltzmann's formulation [48,49], entropy is given by

$$S = k_B \ln(W), \tag{1}$$

where $S$ is the macroscopic thermodynamic entropy, $k_B$ is the Boltzmann constant, and $W$ is the number of accessible microstates (i.e., the degree of disorder). Within the UMT framework, degradation is quantified by a scalar *thermodynamic state index* (TSI), $\phi \in [0, 1)$, defined as a dimensionless measure of the degree of disorder relative to the initial reference state. Accordingly, $\phi$ also serves as a monotonically increasing indicator of accumulated irreversibility. The TSI is defined through the following entropy-based relation [35,36,38]:

$$\phi = \frac{W - W_0}{W} = 1 - \exp\Big(-A_\phi\, s_{\mathrm{tot}}\Big), \qquad A_\phi = \frac{M_s}{\mathcal{R}\,\rho}, \tag{2}$$

where $W_0$ denotes the number of microstates in the initial reference state, $W$ denotes the number of microstates in the current disordered state, and $s_{\mathrm{tot}}$ is the cumulative entropy production per unit bulk volume, with units of $\mathrm{J\,K^{-1}\,m^{-3}}$. Here, $M_s$ is the molar mass of the material ($\mathrm{kg\,mol^{-1}}$), $\mathcal{R}$ is the universal gas constant ($8.314\,\mathrm{J\,mol^{-1}\,K^{-1}}$), and $\rho$ is the mass density of the metal ($\mathrm{kg\,m^{-3}}$). Accordingly, the coefficient $A_\phi$ is obtained directly from expressing Boltzmann entropy in terms of cumulative entropy production per unit bulk volume, ensuring that the product $A_\phi s_{\mathrm{tot}}$ is dimensionless. Eq. (2) further implies that $\phi$ evolves monotonically with cumulative entropy production and approaches unity asymptotically as degradation progresses. When $s_{\mathrm{tot}}$ is expressed as a function of the loading cycle number $N$ in fatigue problems, the TSI evolution can be written as

$$\phi(N) = 1 - \exp\Big(-A_\phi\, s_{\mathrm{tot}}(N)\Big), \tag{3}$$

where $s_{\mathrm{tot}}(N)$ denotes the cumulative entropy production per unit bulk volume accumulated up to cycle $N$.

### 2.2. Entropy generation mechanisms in metals under high cycle fatigue

The evolution of the TSI in Eq. (3) depends on the cumulative entropy production generated during HCF. Expressing the evolution of $\phi$ on a per-cycle basis requires the increment of total entropy production per unit bulk volume and per cycle, denoted by $\Delta s_{\mathrm{tot}}$ (units: $\mathrm{J\,K^{-1}\,m^{-3}\,cycle^{-1}}$). For a block of $N_b$ cycles, the cumulative entropy production per unit bulk volume is updated as

$$s_{\mathrm{tot}}(N + N_b) = s_{\mathrm{tot}}(N) + N_b\, \Delta s_{\mathrm{tot}}. \tag{4}$$

For the irreversible processes considered here, the total entropy production per cycle may, in general, be decomposed into the following contributions [41–43]:

$$\Delta s_{\mathrm{tot}} = \Delta s_{\mathrm{conf}} + \Delta s_{\mathrm{vib}} + \Delta s_{\mathrm{vcd}} + \Delta s_{\mathrm{cond}} + \Delta s_{\mathrm{fric}} + \Delta s_{\mu\mathrm{pl}}, \tag{5}$$

where $\Delta s_{\mathrm{conf}}$, $\Delta s_{\mathrm{vib}}$, and $\Delta s_{\mathrm{vcd}}$ denote the atomic configurational, vibrational, and vacancy-diffusion-related contributions, respectively. On the other hand, $\Delta s_{\mathrm{cond}}$, $\Delta s_{\mathrm{fric}}$, and $\Delta s_{\mu\mathrm{pl}}$ represent entropy generation due to thermal conduction, internal friction associated with rapidly moving dislocations and phonon drag, and microplastic dissipation, respectively [42,43,50]. Among these irreversible mechanisms, microplastic dissipation and internal friction can generate heat and may therefore contribute to temperature evolution, whereas $\Delta s_{\text{cond}}$ is associated with entropy production during heat transport through temperature gradients. By contrast, $\Delta s_{\text{conf}}$, $\Delta s_{\text{vib}}$, and $\Delta s_{\text{vcd}}$ are primarily associated with irreversible changes in the internal material state and do not necessarily produce an observable macroscopic temperature rise.

Previous UMT studies of metallic fatigue have shown that the configurational, vibrational, and vacancy-diffusion contributions are several orders of magnitude smaller than the dominant mechanical-dissipation contributions under comparable conditions [41–43]. For the conventional HCF regime examined here, the loading frequencies are limited to 0.5–10 Hz, where the response is predominantly thermoelastic and significant self-heating or thermal gradients are not typically observed [42,51–53]. By contrast, frequency-induced heating, rapid dislocation motion, and phonon drag may become more important under ultrasonic fatigue conditions [43,53]. The total entropy production per cycle is therefore approximated by the microplastic contribution:

$$\Delta s_{\text{tot}} \approx \Delta s_{\mu\text{pl}}. \tag{6}$$

Accordingly, $\Delta s_{\mu\text{pl}}$ governs the TSI evolution and associated HCF damage accumulation. The omission of the remaining contributions is treated as a regime-specific approximation for the conditions considered here.

### 2.3. Two-scale microplasticity framework and entropy computation

In the HCF/VHCF regimes, the macroscopic response remains nominally elastic, while irreversible cyclic deformation is confined to highly localized microstructural regions [54–58]. Microplasticity may nucleate near stress concentrators or strain-localization sites, including microvoids, nonmetallic inclusions, grain boundaries, persistent slip bands (PSBs), and PSB-associated surface intrusions and extrusions, where small regions of the surrounding matrix undergo cyclic micro-yielding [54,56,58–60]. In FCC metals, this deformation commonly develops through PSBs formed by progressive dislocation localization and rearrangement on favorably oriented slip planes. The resulting intrusions and extrusions intensify local stress and strain concentrations and promote early crystallographic crack initiation [54,61,62]. In BCC metals, cyclic microplasticity is more closely associated with screw-dislocation glide, frequent cross-slip, and heterogeneous dislocation-substructure evolution, with local stresses arising from cross-slip-mediated rearrangement, dislocation pile-ups, and incompatibility [59,63,64]. Rather than explicitly resolving individual stress concentrators or slip systems, the present two-scale model homogenizes the material into a mean-field continuum comprising an elastic matrix and an active microplastic defect phase [42,43,65–67], as illustrated in Fig. 1. Here, $f_v$ denotes the active micro-defect volume fraction, defined as the volume fraction of the active microplastic defect phase within the representative volume element (RVE) and bounded by $0 < f_{v,0} \le f_v \le f_{\text{sat}} < 1$.

Because the thermodynamic state index ($\phi$) represents macroscopic bulk degradation, the microplastic work density accumulated per cycle must be volume-averaged. In the two-phase mean-field framework, the bulk work density $W_{\mu\text{pl}}^{\text{bulk}}$ (units: J m$^{-3}$ per cycle) is the volume-weighted sum of the constituent contributions:

$$W_{\mu\text{pl}}^{\text{bulk}} = f_v\, W_{\mu\text{pl}}^{\text{def}} + (1 - f_v)\, W_{\mu\text{pl}}^{\text{matrix}}, \tag{7}$$

where $W_{\mu\text{pl}}^{\text{def}}$ and $W_{\mu\text{pl}}^{\text{matrix}}$ are the microplastic work densities dissipated in the defect phase and surrounding matrix, respectively. Under the HCF conditions considered here, the matrix remains macroscopically elastic, such that $W_{\mu\text{pl}}^{\text{matrix}} = 0$. The bulk dissipation is therefore governed entirely by the localized defect zones, and Eq. (7) reduces to

$$W_{\mu\text{pl}}^{\text{bulk}} = f_v\, W_{\mu\text{pl}}^{\text{def}}. \tag{8}$$

The defect phase is a localized yielding subdomain of the base matrix and therefore shares the same macroscopic elastic moduli ($E$, $\mu$). This motivates the use of a Kröner-type inclusion formulation [68–70]. Under the applied macroscopic stress tensor $\boldsymbol{\Sigma}$ (units: MPa), the total macroscopic strain tensor $\boldsymbol{E}$ is decomposed as

$$\boldsymbol{E} = \mathbb{S} : \boldsymbol{\Sigma} + f_v\, \epsilon_p^{\mu}, \tag{9}$$

where $\mathbb{S}$ is the fourth-order elastic compliance tensor and $\epsilon_p^{\mu}$ is the microplastic strain tensor confined to the defect phase. The corresponding micro-stress is

$$\boldsymbol{\sigma}^{\mu} = \boldsymbol{\Sigma} - 2\mu(1 - \beta)(1 - f_v)\, \epsilon_p^{\mu}, \tag{10}$$

where $\mu$ is the shear modulus and $\beta$ is the Eshelby elastic accommodation factor determined by Poisson's ratio $\nu$. The factor $\beta$ represents the elastic restraint imposed by the surrounding matrix and governs how localized microplastic strain modifies the micro-stress relative to the applied macroscopic stress.

In the earlier BCC-based formulation, the cumulative entropy production associated with localized microplastic dissipation up to cycle $N$ was expressed in the time domain as [42–44]

$$s_{\mu\text{pl}}(N) = \int_{t_0}^{t_N} \frac{1}{T(t)}\, \dot{W}_{\mu\text{pl}}^{\text{bulk}}(t)\, \mathrm{d}t = \Psi_f \int_{t_0}^{t_N} \frac{1}{T(t)}\, \phi f_v\, \boldsymbol{\sigma}^{\mu} : \dot{\epsilon}_p^{\mu}\, \mathrm{d}t. \tag{11}$$

Here, $t_0$ and $t_N$ correspond to cycle counts 0 and $N$, respectively, and $\dot{W}_{\mu\text{pl}}^{\text{bulk}} = \phi f_v \dot{W}_{\mu\text{pl}}^{\text{def}}$, with $\dot{W}_{\mu\text{pl}}^{\text{def}} = \boldsymbol{\sigma}^{\mu} : \dot{\epsilon}_p^{\mu}$. The factor $\phi f_v$ represents the degradation-dependent active fraction of the defect phase, $T(t)$ is the instantaneous absolute temperature (units: K), and $\Psi_f$ is a dimensionless correction factor introduced in earlier BCC-based ultrasonic-fatigue formulations to account for the frequency dependence of screw-dislocation cross-slip. For conventional HCF, $\Psi_f$ may be taken as unity.

Although Eq. (11) accommodates general time-dependent loading histories within the earlier framework, explicit integration over millions of HCF cycles is computationally impractical. Under steady periodic loading without significant global self-heating, the entropy increment per cycle can be expressed as the following closed-cycle contour integral in micro-stress-microplastic-strain space:

$$\Delta s_{\mu\text{pl}} = \frac{1}{T}\, \Psi_f\, \phi f_v \oint \boldsymbol{\sigma}^{\mu} : \mathrm{d}\epsilon_p^{\mu}. \tag{12}$$

The contour integral gives the defect-phase microplastic energy dissipated per cycle, while $\phi f_v$ converts it to the corresponding bulk-averaged contribution. In the numerical implementation, stresses in MPa are converted using $1\,\text{MPa} = 10^6\,\text{J}\,\text{m}^{-3}$, ensuring that the dissipation is expressed as energy per unit volume. In the FCC formulation developed below, the degradation-dependent active-volume scaling is replaced by an explicitly bounded evolution law for $f_v(\phi)$, such that $W_{\mu\text{pl}}^{\text{bulk}} = f_v(\phi) W_{\mu\text{pl}}^{\text{def}}$.

### 2.4. Limitations of the earlier microplastic entropy formulation

Although the earlier microplastic entropy formulation provided an efficient framework for HCF life prediction in BCC metals, its extension to FCC materials requires several assumptions to be reconsidered:

1. *Dependence on a distinct micro-yielding threshold.* The previous model activated microplasticity only when the applied stress amplitude exceeded a prescribed fatigue limit or micro-yielding stress $\sigma_y^{\mu}$. Although suitable for many BCC steels, this assumption is less appropriate for FCC metals such as aluminum alloys, in which small but nonzero microplastic strain may accumulate at low amplitudes and a strict endurance limit is generally absent.
2. *Need for a more general description of rate and thermal effects.* The earlier formulation introduced an extrinsic frequency coefficient, $\Psi_f$, to represent the inverse relation between screw-dislocation cross-slip probability and loading frequency in BCC metals. This correction cannot be directly transferred to FCC metals, where

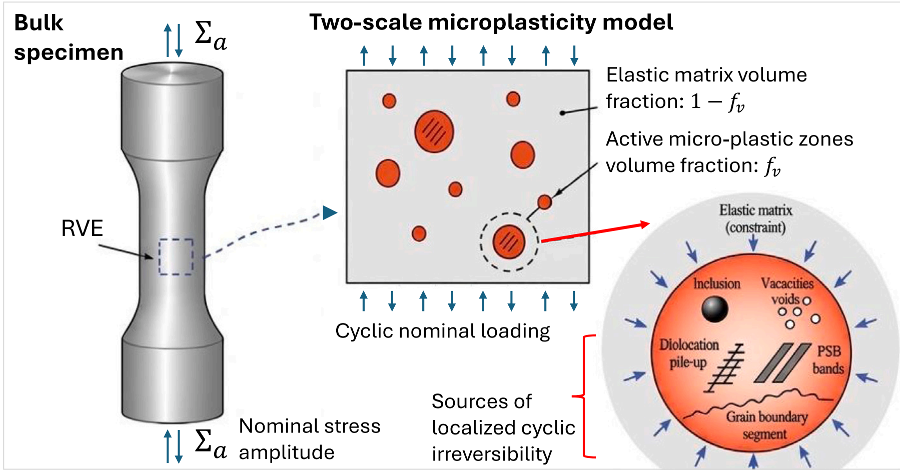


**Fig. 1.** Schematic diagram of the two-scale microplasticity model.

localized cyclic microplasticity is not governed by the same cross-slip mechanism. Moreover, $\Psi_f$ does not explicitly represent the effects of temperature, strain rate, activation energy, or activation volume on microplastic slip.

3. *Assumption of cycle-invariant defect-scale hysteresis.* The earlier formulation assumed that the hysteresis loop at each defect site remained stabilized at a given stress amplitude, while only the active micro-defect fraction evolved with the thermodynamic state index, $\phi$. Treating the localized microplastic work density, $W_{\mu\mathrm{pl}}^{\mathrm{def}}$, as cycle-invariant therefore neglected possible hysteresis evolution caused by progressive microstructural rearrangement and degradation, limiting the coupling between mechanical dissipation and the evolving internal state.

### 2.5. Proposed microplasticity model for FCC metals

To extend the framework to FCC metals, the revised model employs an Eyring-type thermally activated flow law [71,72] without an explicitly imposed micro-yielding threshold. The active micro-defect fraction, $f_v$, and micro-kinematic hardening modulus, $h$, are governed by bounded evolution laws defined by their initial and saturation values and corresponding shape parameters. The model therefore represents rate-dependent localized slip that can persist even at very low stress amplitudes, together with the evolution of active micro-defect regions and defect-scale kinematic resistance as fatigue degradation progresses.

#### 2.5.1. Evolution of the active micro-defect fraction

Within the proposed two-scale framework, the active micro-defect fraction $f_v$ evolves with the thermodynamic degradation state $\phi$, representing the progressive multiplication and spatial broadening of localized cyclic-slip regions in favorably oriented grains. Its evolution is expressed by the bounded mapping

$$f_v(\phi) = f_{v,0} + \left(f_{\mathrm{sat}} - f_{v,0}\right) g_v(\phi), \tag{13}$$

where $f_{v,0}$ and $f_{\mathrm{sat}}$ denote the initial and saturated active micro-defect fractions, respectively. The transition function satisfies $g_v(0) = 0$ and $g_v(1) = 1$. The benchmark adopts the power form $g_v(\phi) = \phi^{a_{\mathrm{fv}}}$, with $a_{\mathrm{fv}} = 1$. To evaluate sensitivity to the assumed transition shape, two bounded alternatives with the same endpoints are considered. The normalized-exponential form $g_v(\phi) = (1 - e^{-k\phi})/(1 - e^{-k})$, using the representative value $k = 4$, concentrates most of the increase in $f_v$ at low $\phi$ before gradually approaching saturation, whereas the smoothstep form $g_v(\phi) = 3\phi^2 - 2\phi^3$ evolves most rapidly at intermediate $\phi$. Nevertheless, experimental measurements of active-slip or persistent-slip-band fractions are required to identify the appropriate transition law and its shape parameter.

#### 2.5.2. Microplastic driving force and kinematic hardening

To represent the internal resistance from localized dislocation interactions within the defect phase, the backstress tensor $\boldsymbol{\alpha}$ is introduced through a simplified linear kinematic-hardening relation: $\boldsymbol{\alpha} = \frac{2}{3} h\, \epsilon_p^{\mu}$, where $h$ is the micro-kinematic hardening modulus (units: MPa) [73, 74]. The effective driving tensor for microplastic flow is defined as the difference between the deviatoric micro-stress, $\boldsymbol{s}^{\mu} = \mathrm{dev}(\boldsymbol{\sigma}^{\mu})$, and the backstress. Substitution of Eq. (10) gives [42,68,70]

$$\mathbf{A} = \boldsymbol{s}^{\mu} - \boldsymbol{\alpha} = \mathrm{dev}(\boldsymbol{\Sigma}) - \left[2\mu(1-\beta)(1-f_v) + \frac{2}{3}h\right] \epsilon_p^{\mu}. \tag{14}$$

Eq. (14) represents the instantaneous defect-scale resistance to localized slip, with the backstress generated by accumulated microplastic strain opposing the driving force **A**. Many cyclically loaded FCC metals also exhibit progressive softening or reduced hardening capacity due to dislocation rearrangement, slip localization, and persistent slip-structure development [75,76]. Depending on the material state and loading conditions, these evolving structures may appear as PSB ladders, wall–channel arrangements, or cellular substructures [77–79].

To represent this long-term evolution in reduced form, the present model assumes that the micro-kinematic hardening modulus decreases with increasing thermodynamic degradation. Accordingly, $h$ evolves as

$$h(\phi) = h_0 + \left(h_{\mathrm{sat}} - h_0\right) g_h(\phi), \tag{15}$$

where $h_0$ and $h_{\mathrm{sat}}$ are the initial and saturated micro-kinematic hardening moduli, respectively, and $g_h(\phi)$ follows the bounded transition functions introduced above. The AA7075-T651 benchmark uses $h_{\mathrm{sat}} < h_0$ to represent progressive cyclic softening. This reduction is physically associated with repeated dislocation interactions during cyclic slip localization, including cross-slip, annihilation, and the development of dipolar or wall-like structures within persistent slip bands. These dissipative rearrangement processes reduce the defect-scale resistance to subsequent slip while contributing to thermodynamic disorder and entropy production. Setting $h_{\mathrm{sat}} = h_0$ gives a constant micro-kinematic hardening modulus, whereas $h_{\mathrm{sat}} > h_0$ permits an increasing micro-kinematic hardening modulus for materials exhibiting cyclic hardening; these cases require validation against corresponding cyclic-response data.

#### 2.5.3. Thermally activated flow law and crystallographic bridge

FCC plastic deformation occurs through crystallographic slip on $\{111\}\langle 110\rangle$ systems, but the present mean-field model does not resolve individual slip systems. Instead, the continuum defect-scale driving tensor is represented by the invariant measure $\sqrt{3/2}\|\mathbf{A}\|$ and projected onto representative FCC slip systems using an effective Schmid factor $\bar{m}$. The effective resolved shear stress is therefore

$$\tau_{\mathrm{eff}} = \bar{m}\sqrt{\frac{3}{2}}\|\mathbf{A}\|, \tag{16}$$

where $\|\cdot\|$ denotes the Frobenius norm.

Microplastic flow follows Eyring-type thermally activated kinetics [80–82]:

$$\dot{\gamma} = \dot{\gamma}_0 \exp\left(-\frac{\Delta F_0}{k_B T}\right) \sinh\left(\frac{V_{\text{act}}\,\tau_{\text{eff}}}{k_B T}\right), \tag{17}$$

where $\dot{\gamma}_0$ is the reference shear-rate prefactor, $\Delta F_0$ is the activation energy, $V_{\text{act}}$ is the activation volume, and $k_B$ is Boltzmann's constant. A key feature of the FCC formulation is that $\tau_{\text{eff}}$ contains no subtractive threshold stress. This reflects the comparatively low lattice friction of FCC crystals, allowing localized microplastic slip to vary smoothly with stress even at small nonzero amplitudes, consistent with the absence of a distinct endurance limit in many FCC systems. In contrast, the non-planar screw-dislocation cores in BCC crystals produce a significant Peierls barrier [83–86]. BCC formulations therefore often introduce a threshold resistance $\tau_\mu$ and define an effective overstress such as $\langle \tau_{\text{eff}} - \tau_\mu \rangle$. The present formulation therefore represents rate dependence directly through thermally activated kinetics without imposing an explicit micro-yielding threshold [41–44].

Eq. (17) also provides a constitutive interpretation of loading-frequency effects. At fixed stress amplitude and temperature, increasing the frequency shortens the loading period and therefore reduces the thermally activated slip accumulated per cycle. Differences in lattice resistance, dislocation-core structure, activation energy, and activation volume can consequently produce material-dependent frequency responses in BCC and FCC metals. In the present FCC formulation, frequency enters through the time integration of the Eyring flow rate, replacing the scalar frequency correction used in earlier BCC-oriented formulations.

### 2.5.4. Strain update and second-law consistency

To derive the microplastic strain update and entropy production consistently with the second law, the following assumptions are adopted: (1) the surrounding matrix remains elastic, and dissipation is confined to the defect phase; (2) the macroscopic stress $\boldsymbol{\Sigma}$ enters through the localization relations for $\boldsymbol{\sigma}^\mu$ and $\mathbf{A}$, with the bulk-averaged dissipation rate given by $f_v \mathcal{D}^\mu$, where $\mathcal{D}^\mu$ is the local mechanical dissipation rate per unit active micro-defect volume; and (3) the response is isothermal and infinitesimal-strain. The general case with evolving $h$ is derived first and then specialized to the stabilized-cycle solve, during which $h$ is fixed.

The defect-scale strain is additively decomposed as

$$\boldsymbol{\epsilon}^\mu = \boldsymbol{\epsilon}^\mu_e + \boldsymbol{\epsilon}^\mu_p. \tag{18}$$

For the adopted linear backstress relation, the hardening internal variable is taken as the microplastic strain, $\boldsymbol{\xi} = \boldsymbol{\epsilon}^\mu_p$. The Helmholtz free-energy density per unit active micro-defect volume is postulated as

$$\psi^\mu = \frac{1}{2}\boldsymbol{\epsilon}^\mu_e : \mathbb{C} : \boldsymbol{\epsilon}^\mu_e + \frac{1}{3} h\, \boldsymbol{\xi} : \boldsymbol{\xi}. \tag{19}$$

With $\bar{\epsilon}^\mu_p = \sqrt{(2/3)\boldsymbol{\epsilon}^\mu_p : \boldsymbol{\epsilon}^\mu_p}$, the kinematic contribution becomes $\psi^\mu_k = (1/2)h(\bar{\epsilon}^\mu_p)^2$. The associated stress and backstress are

$$\boldsymbol{\sigma}^\mu = \frac{\partial \psi^\mu}{\partial \boldsymbol{\epsilon}^\mu_e} = \mathbb{C} : \boldsymbol{\epsilon}^\mu_e, \qquad \boldsymbol{\alpha} = \frac{\partial \psi^\mu_k}{\partial \boldsymbol{\xi}} = \frac{2}{3} h \boldsymbol{\xi} = \frac{2}{3} h \boldsymbol{\epsilon}^\mu_p. \tag{20}$$

Under isothermal conditions without thermal gradients, the local Clausius–Duhem inequality reduces to

$$\mathcal{D}^\mu = \boldsymbol{\sigma}^\mu : \dot{\boldsymbol{\epsilon}}^\mu - \dot{\psi}^\mu \ge 0. \tag{21}$$

Allowing $h$ to evolve and using Eqs. (18)–(20) gives

$$\begin{aligned} \mathcal{D}^\mu &= \boldsymbol{\sigma}^\mu : \dot{\boldsymbol{\epsilon}}^\mu_p - \boldsymbol{\alpha} : \dot{\boldsymbol{\epsilon}}^\mu_p - \frac{1}{3}\dot{h}\, \boldsymbol{\epsilon}^\mu_p : \boldsymbol{\epsilon}^\mu_p \\ &= \mathbf{A} : \dot{\boldsymbol{\epsilon}}^\mu_p - \frac{1}{3}\dot{h}\, \boldsymbol{\epsilon}^\mu_p : \boldsymbol{\epsilon}^\mu_p \ge 0, \end{aligned} \tag{22}$$

where $\mathbf{A} = \boldsymbol{s}^\mu - \boldsymbol{\alpha}$. Microplastic incompressibility, $\mathrm{tr}(\dot{\boldsymbol{\epsilon}}^\mu_p) = 0$, eliminates hydrostatic stress work. Thus, $\mathbf{A}$ is work-conjugate to microplastic flow, while the second term represents the energetic contribution from the evolution of $h$.

During each stabilized-cycle solve, $h$ is fixed, so Eq. (22) reduces to

$$\mathcal{D}^\mu = \mathbf{A} : \dot{\boldsymbol{\epsilon}}^\mu_p. \tag{23}$$

To bridge the continuum defect response and crystallographic slip, their work increments are equated:

$$\mathbf{A} : \Delta\boldsymbol{\epsilon}^\mu_p = \tau_{\text{eff}} \Delta\gamma, \tag{24}$$

where $\Delta\gamma = \dot{\gamma}\Delta t$ and $\tau_{\text{eff}} = \bar{m}\sqrt{3/2}\|\mathbf{A}\|$. Assuming that the microplastic strain increment is aligned with $\mathbf{A}$ gives

$$\Delta\boldsymbol{\epsilon}^\mu_p = \bar{m}\sqrt{\frac{3}{2}}\,\Delta\gamma \frac{\mathbf{A}}{\|\mathbf{A}\|}, \qquad \|\mathbf{A}\| > 0, \tag{25}$$

with $\Delta\boldsymbol{\epsilon}^\mu_p = \mathbf{0}$ at $\mathbf{A} = \mathbf{0}$. Because the Eyring relation gives $\Delta\gamma \ge 0$, this update satisfies $\mathbf{A} : \Delta\boldsymbol{\epsilon}^\mu_p = \tau_{\text{eff}}\Delta\gamma \ge 0$. The defect-scale microplastic work dissipated per cycle and corresponding bulk entropy increment are therefore

$$W^{\text{def}}_{\mu\text{pl}} = \oint \mathbf{A} : \mathrm{d}\boldsymbol{\epsilon}^\mu_p = \oint \tau_{\text{eff}}\,\mathrm{d}\gamma \ge 0, \qquad \Delta s_{\mu\text{pl}} = \frac{f_v W^{\text{def}}_{\mu\text{pl}}}{T} \ge 0. \tag{26}$$

For a closed stabilized cycle with fixed $h$, $\oint \boldsymbol{\alpha} : \mathrm{d}\boldsymbol{\epsilon}^\mu_p = \Delta\psi^\mu_k = 0$, so $\oint \boldsymbol{s}^\mu : \mathrm{d}\boldsymbol{\epsilon}^\mu_p = W^{\text{def}}_{\mu\text{pl}}$. In the present HCF calculations, the separate dissipation contribution associated with the evolution of $h$ is treated as negligible because the microplastic strain remains small and $h$ evolves gradually. The updated value of $h$ nevertheless modifies $\boldsymbol{\alpha}$ and $\mathbf{A}$, thereby affecting subsequent microplastic-flow dissipation.

## 3. Numerical model implementation

### 3.1. Computation scheme for microplasticity entropy and TSI evolution

To simulate the extreme cycle counts of the HCF and VHCF regimes, a hierarchical cycle/block integration scheme integrates the intra-cycle microplastic response and advances the global degradation state over adaptive macroscopic blocks $N_b$:

1. Initialize the global variables and defect-scale tensors:

   $$N = 0, \qquad s_{\text{tot}} = 0, \qquad \phi = \phi_0 = 0, \qquad \boldsymbol{\epsilon}^\mu_p = \mathbf{0}, \qquad \boldsymbol{\alpha} = \mathbf{0}.$$

2. For a prescribed macroscopic stress amplitude $\boldsymbol{\Sigma}_a$, mean stress $\boldsymbol{\Sigma}_m$, and frequency $f$, discretize the loading period into $n$ increments. When the loading condition is prescribed by the maximum stress and stress ratio,

   $$\Sigma_a = \frac{1-R}{2}\Sigma_{\max}, \qquad \Sigma_m = \frac{1+R}{2}\Sigma_{\max}.$$

   The loading history is

   $$\boldsymbol{\Sigma}(t) = \boldsymbol{\Sigma}_m + \boldsymbol{\Sigma}_a \sin(2\pi f t),$$

   yielding the discrete sequence $\{\boldsymbol{\Sigma}_i\}_{i=1}^{n+1}$.
3. At the start of block $k$, update the state-dependent parameters using $\phi_k$ and hold them fixed over the block:

   $$f_{v,k} = f_{v,0} + \left(f_{\text{sat}} - f_{v,0}\right)\phi_k^{a_{\text{fv}}}, \qquad h_k = h_0 - \left(h_0 - h_{\text{sat}}\right)\phi_k^{a_h}.$$

4. Integrate the microplastic response over the $n$ increments of duration $\Delta t$ until the cyclic microplastic work stabilizes. For each increment $i \to i+1$:
   (a) Evaluate the midpoint macroscopic stress:

   $$\boldsymbol{\Sigma}_{\text{mid}} = \frac{1}{2}\left(\boldsymbol{\Sigma}_i + \boldsymbol{\Sigma}_{i+1}\right).$$

   (b) Compute the defect-scale driving tensor:

   $$\mathbf{A} = \mathrm{dev}\left(\boldsymbol{\Sigma}_{\text{mid}}\right) - \left[2\mu(1-\beta)(1-f_{v,k}) + \frac{2}{3}h_k\right]\boldsymbol{\epsilon}^\mu_{p,i}.$$

(c) Evaluate the effective resolved shear stress:

$$\tau_{\mathrm{eff}} = \bar{m}\sqrt{\frac{3}{2}}\|\mathbf{A}\|.$$

(d) Compute the crystallographic slip increment and update the microplastic strain:

$$\Delta\epsilon_p^{\mu} = \dot{\gamma}(\tau_{\mathrm{eff}})\Delta t\left(\bar{m}\sqrt{\frac{3}{2}}\right)\frac{\mathbf{A}}{\|\mathbf{A}\|}, \qquad \epsilon_{p,i+1}^{\mu} = \epsilon_{p,i}^{\mu} + \Delta\epsilon_p^{\mu}.$$

(e) Accumulate the work-conjugate defect-scale dissipation over the stabilized cycle:

$$W_{\mu\mathrm{pl}}^{\mathrm{def}} = \sum_{i=1}^{n}\mathbf{A}_i : \Delta\epsilon_{p,i}^{\mu} = \sum_{i=1}^{n}\tau_{\mathrm{eff},i}\Delta\gamma_i \geq 0.$$

5. Evaluate the cyclic microplastic work and entropy production:

$$W_{\mu\mathrm{pl}}^{\mathrm{bulk}} = f_{v,k}W_{\mu\mathrm{pl}}^{\mathrm{def}}, \qquad \Delta s_{\mathrm{tot}} = \frac{f_{v,k}W_{\mu\mathrm{pl}}^{\mathrm{def}}}{T}.$$

Determine an adaptive block size $N_b$ from the target resolutions $\Delta\phi_{\mathrm{target}}$ and $\Delta f_{v,\mathrm{target}}$. The instantaneous evolution rates are

$$\frac{d\phi}{dN} = A_{\phi}(1-\phi)\Delta s_{\mathrm{tot}}, \qquad \frac{df_v}{dN} = \left(f_{\mathrm{sat}} - f_{v,0}\right)\frac{dg_v}{d\phi}\frac{d\phi}{dN}.$$

For the benchmark power law, $dg_v/d\phi = a_{\mathrm{fv}}\phi^{a_{\mathrm{fv}}-1}$. The corresponding candidate block sizes are

$$N_{b,\phi} = \frac{\min\left(\Delta\phi_{\mathrm{target}}, \phi_{\mathrm{cr}} - \phi\right)}{d\phi/dN}, \qquad N_{b,f_v} = \frac{\Delta f_{v,\mathrm{target}}}{df_v/dN}.$$

The candidate block size is

$$N_{b,\mathrm{candidate}} = \max\left[1, \left\lfloor \min\left(N_{b,\phi}, N_{b,f_v}, N_{b,\max}\right)\right\rfloor\right].$$

Near failure,

$$N_{b,\mathrm{fail}} = \left\lceil \frac{s_{\mathrm{cr}} - s_{\mathrm{tot}}}{\Delta s_{\mathrm{tot}}} \right\rceil, \qquad N_b = \min\left(N_{b,\mathrm{candidate}}, N_{b,\mathrm{fail}}\right).$$

This records failure at the first integer cycle reaching $s_{\mathrm{cr}}$, with a crossing error below one equivalent cycle.

6. Advance the global state over the selected block:

$$s_{\mathrm{tot}} \leftarrow s_{\mathrm{tot}} + N_b\Delta s_{\mathrm{tot}}, \qquad N \leftarrow N + N_b, \qquad \phi = 1 - \exp\left(-A_{\phi}s_{\mathrm{tot}}\right).$$

7. Repeat Steps 3–6 until

$$\phi \geq \phi_{\mathrm{cr}},$$

and record $N$ as the predicted fatigue life.

The accelerated block scheme is most appropriate for fully reversed loading, where the local response rapidly approaches a periodic loop without sustained mean-strain drift. It also applies when the initial transient response under mean stress is brief and local ratcheting rapidly decays to a stabilized cycle. However, progressive long-term ratcheting would require a history-carrying cycle-by-cycle solver. The computational scheme is summarized in Fig. 2.

### 3.2. Inputs for the numerical model

The proposed microplasticity entropy model requires prescribed loading conditions, material constants, theoretically derived quantities, literature-based kinetic parameters, and parameters associated with assumed microstructural parameter evolution laws. Their identification strategy is summarized in Table 1, while Section 4.1 provides the values used in the benchmark study.

The loading variables $(T, \Sigma_a, \Sigma_m, R, f)$ are prescribed by the test conditions, while $E$, $\nu$, $\rho$, $M_s$, and the universal gas constant $\mathcal{R}$ are obtained from standard material data or fundamental constants. Here, $R$ denotes the stress ratio.

**Table 1**
Summary of model parameters and their identification strategy, ordered by direct identifiability.

| Parameter group | Source and identification strategy |
|---|---|
| $T, \Sigma_a, \Sigma_m, R, f$ | Prescribed loading conditions and thermal environment. |
| $E, \nu, \rho, M_s, \mathcal{R}$ | Standard material databases, alloy composition, direct measurement, or fundamental constants. |
| $\beta, \bar{m}$ | Theoretical estimates derived from inclusion theory and FCC crystallographic considerations. |
| $\Delta F_0, V_{\mathrm{act}}, \dot{\gamma}_0$ | Selected from literature-reported dislocation-kinetics ranges or estimated from independent rate-sensitivity data. The resulting baseline set is held fixed for subsequent forward calculations. |
| $f_{v,0}, f_{\mathrm{sat}}$ | Microstructural estimates based on the initial inclusion or microporosity volume fraction and the admissible fraction of slip-active grains. |
| $a_{\mathrm{fv}}, a_h, h_0, h_{\mathrm{sat}}$ | Parameters of the assumed microstructural parameter evolution laws, selected with reference to cyclic deformation characteristics and examined through sensitivity analysis. |
| $\phi_{\mathrm{cr}}$ | Critical thermodynamic state index associated with final fracture and examined through sensitivity analysis. |

The Eshelby elastic accommodation factor $\beta$ is determined from inclusion theory [68,87] for a spherical defect embedded in an isotropic elastic matrix:

$$\beta = \frac{2(4-5\nu)}{15(1-\nu)}. \tag{27}$$

Within the two-scale localization relation, $\beta$ enters through $2\mu(1-\beta)(1-f_v)$ and quantifies the elastic constraint imposed by the surrounding matrix on the localized microplastic strain. The isotropic elastic idealization is adopted because the bulk response remains nominally elastic under HCF, while the local microplastic response is governed separately by the orientation factor, Eyring kinetics, and micro-kinematic hardening modulus.

The effective Schmid factor $\bar{m}$ is selected from FCC crystallographic considerations [88]. The parameters $\Delta F_0$, $V_{\mathrm{act}}$, and $\dot{\gamma}_0$ are treated as effective room-temperature quantities and selected from literature-reported ranges for dislocation-glide kinetics or estimated from independent rate-sensitivity data [81,82]. The reference shear-rate prefactor may be estimated from the Orowan-type relation [80,88]

$$\dot{\gamma}_0 = \rho_m b^2 \nu_D, \tag{28}$$

where $\rho_m$ is the mobile dislocation density, $b$ is the magnitude of the Burgers vector, and $\nu_D$ is the Debye attempt frequency.

The remaining parameters governing defect evolution and the final-state criterion, namely $f_{v,0}$, $f_{\mathrm{sat}}$, $a_{\mathrm{fv}}$, $a_h$, $h_0$, $h_{\mathrm{sat}}$, and $\phi_{\mathrm{cr}}$, are less directly identifiable and are therefore estimated from microstructural considerations, inferred from cyclic response characteristics, or introduced as benchmark assumptions to be examined later through sensitivity analysis in Section 4.4.

It should be noted that the literature-based parameter set adopted for the cylindrical $R = -1$ benchmark was applied across all benchmark stress amplitudes in Section 4.1 and retained for the prescribed stress-ratio scenarios in Section 4.2, without pointwise or condition-specific refitting. For the smooth flat dog-bone specimen assessment in Section 4.3, a corresponding literature-based parameter set was adopted for the plate $R = -1$ cases and subsequently retained for prediction of the $R \approx 0$ results.

## 4. Numerical results and discussion

The numerical assessment uses AA7075-T651 as a benchmark for FCC alloys. The material properties and loading conditions for the fully

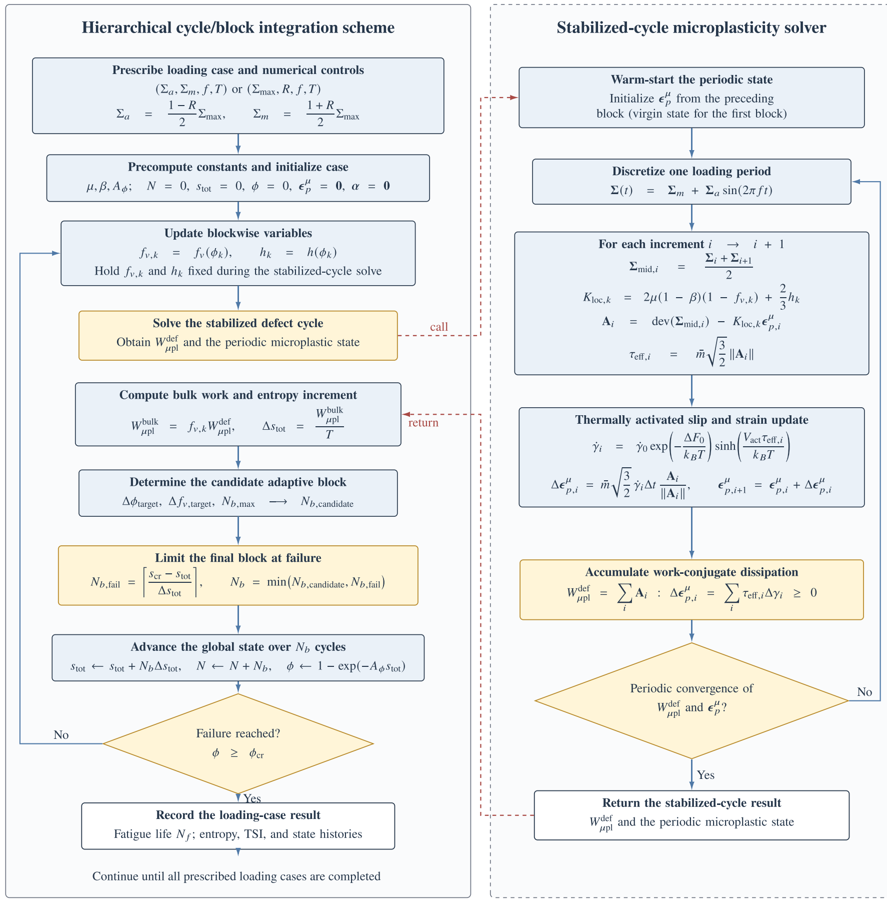

**Fig. 2.** Computational scheme of the UMT-based two-scale microplasticity model.

reversed smooth cylindrical dog-bone benchmark are introduced first, followed by the simulation parameter set and the predicted defect-scale hysteresis, evolution of the microstructural state variables, entropy production, and fatigue lives. Additional stress-ratio scenarios examine the model's numerical capability, while comparisons with smooth flat dog-bone experiments at $R = -1$ and $R \approx 0$ identify the present limitations under non-fully reversed loading. Parameter sensitivity and interaction, alternative microstructural parameter evolution laws, and validation limits are then discussed.

### *4.1. Benchmark simulation of fully reversed HCF in smooth cylindrical dog-bone specimens*

#### *4.1.1. Benchmark experiments and directly adopted inputs*

The primary benchmark adopts the fully reversed uniaxial fatigue experiments on AA7075-T651 reported by Zhao and Jiang [89]. The tests used smooth cylindrical dog-bone specimens in room-temperature air. The material contains equiaxed grains of approximately 10–40 μm and hard constituent particles of $Cr_2Mg_3Al_{18}$ and $(Fe,Mn)Al_6$ [89]. Table 2 summarizes the material properties and prescribed loading conditions, while Table 3 lists the exact stress-amplitude and loading-frequency pairs. The benchmark is treated within the HCF framework because the specimens remain predominantly nominally elastic. However, the highest-amplitude cases, with lives near $10^3$ cycles and stresses close to macroscopic yielding, are more appropriately regarded as lying within the LCF–HCF transition regime.

#### *4.1.2. Parameter values for the benchmark simulation*

Following the identification strategy outlined in Section 3.2, Table 4 summarizes the remaining constitutive and kinetic parameters and the parameters defining the microstructural parameter evolution laws used for the AA7075-T651 benchmark.

**Table 2**
Material properties and experimental loading inputs for AA7075-T651 based on [89].

| Parameter | Value/Description |
|---|---|
| $E$ | Elastic modulus: 71.7 GPa |
| $\nu$ | Poisson ratio: 0.306 |
| $\Sigma_{0.2}$ | Macroscopic yield stress: 501 MPa |
| $T$ | Temperature: 298 K |
| $R$ | Stress ratio: −1 |
| $f$ | Case-specific loading frequency: 0.5–10 Hz; see Table 3 |
| $\Sigma_a$ | Stress amplitude: < 501 MPa |

#### *4.1.3. High cycle fatigue life prediction using the UMT framework*

Based on the prescribed material parameters, the model predicts cyclic responses at both the macroscopic and defect scales. Figs. 3–7 present representative results at different macroscopic stress amplitudes. Subplots (a) compare the global elastic-matrix response with the localized defect-phase response. Because the applied stress amplitudes remain below the macroscopic yield strength of 501 MPa, the matrix exhibits a linear elastic stress–strain relation, whereas the defect phase develops a finite hysteresis loop. This behavior illustrates the coexistence of macroscopic elasticity and localized microplasticity in the two-scale formulation. Subplots (b) show the total defect-phase hysteresis loops, including both elastic and microplastic contributions. These loops arise from crystallographic slip within the localized defect phase and represent the corresponding energy dissipation. Their progressive widening reflects the reduction in the micro-kinematic hardening modulus during fatigue. Subplots (c) isolate the microplastic component and therefore provide a direct representation of the irreversible strain responsible for entropy production and degradation.

**Table 3**
Reported stress amplitudes and corresponding loading frequencies [89].

| Test case | 1 | 2 | 3 | 4 | 5 | 6 | 7 | 8 | 9 | 10 |
|---|---|---|---|---|---|---|---|---|---|---|
| $\Sigma_a$ (MPa) | 485.5 | 400.1 | 361.6 | 349.7 | 299.6 | 240.0 | 214.9 | 210.1 | 200.2 | 150.0 |
| $f$ (Hz) | 0.5 | 0.5 | 1 | 1 | 1 | 2 | 10 | 10 | 6 | 10 |

**Table 4**
Benchmark-specific parameters for the constitutive, kinetic, and microstructural parameter evolution laws of AA7075-T651.

| Parameter | Adopted value | Physical interpretation and source |
|---|---|---|
| $\bar{m}$ | 0.327 | Effective Schmid factor. For FCC alloys, the average Taylor factor is commonly taken as 3.06 [88,90–92]; therefore, $\bar{m}$ is computed as its direct reciprocal. |
| $\beta$ | 0.47 | Eshelby elastic accommodation factor, derived directly from Eq. (27). |
| $\Delta F_0$ | $1.005\times10^{-19}$ J (0.627 eV) | Effective activation energy for localized cyclic microplasticity in FCC aluminum. Literature reports values on the order of 1.3 eV for macroscopic flow stress based on dislocation-glide barrier parameterization [81]. Since the present model represents defect-scale cyclic microplasticity rather than macroscopic yielding, $\Delta F_0 = 0.627$ eV is adopted as an effective room-temperature value within the literature-reported range. |
| $V_{\mathrm{act}}$ | $1.17\times10^{-28}$ m$^3$ | Effective activation volume for thermally activated slip. Set to $5b^3$ to reflect restricted dislocation mobility in the peak-aged T651 temper, consistent with the experimental lower range reported for highly constrained AA7075 [93]. |
| $\dot{\gamma}_0$ | $10^7$ s$^{-1}$ | Reference shear-rate prefactor. Estimated from Eq. (28) using $\rho_m = 10^{13}$ m$^{-2}$ [94–96] and $\nu_D = 10^{13}$ s$^{-1}$ [97]. The adopted $\rho_m$ level is consistent with reported values for AA7075 and other aluminum alloys. |
| $f_{v,0}$ | 0.02 | Initial active micro-defect fraction, selected to be consistent with the approximately 2% coarse constituent-particle population reported for AA7075-T651 [98,99]. This choice reflects the role of coarse constituent particles as a dominant population for initial fatigue-crack initiation [54,89]. |
| $f_{\mathrm{sat}}$ | 0.15 | Saturated active micro-defect fraction. Ideally, this parameter should be inferred from the stabilized cyclic microstructure by estimating the fraction of localized cyclic-slip regions in FCC metals [100,101]. Because no literature directly supports an exact value for AA7075-T651, $f_{\mathrm{sat}} = 0.15$ is adopted as a physically reasonable upper-bound assumption guided by earlier numerical studies. |
| $a_{\mathrm{fv}}, a_h$ | 1, 1 | Shape exponents for the active micro-defect fraction and micro-kinematic hardening modulus. The benchmark assumes linear variations of $f_v$ and $h$ with TSI in Eqs. (13) and (15), respectively. Alternative bounded microstructural parameter evolution laws are examined later to quantify the associated uncertainty. |
| $h_0$ | 5000 MPa | Initial micro-kinematic hardening modulus. Derived from macroscopic multicomponent cyclic-plasticity calibrations for AA7075-T6 [102] and scaled down to account for the lower strengthening coefficients associated with localized cyclic slip within the defect phase [70,101]. |
| $h_{\mathrm{sat}}$ | 150 MPa | Saturated micro-kinematic hardening modulus. Derived from bulk cyclic calibrations [102] using the same micromechanical reduction adopted for the localized defect phase [70,101]. |
| $\phi_{\mathrm{cr}}$ | 0.99 | Critical TSI at macroscopic failure, taken as a representative high cycle fatigue failure threshold for metals in previous UMT studies [41–44]. |

The loop size depends strongly on the applied stress amplitude. As the amplitude decreases from 485.5 to 214.9 MPa, the total defect-phase loops become narrower and approach a nearly linear response, while their progressive softening becomes less pronounced. The lower effective driving stress $\tau_{\mathrm{eff}}$ suppresses the thermally activated slip rate, reducing the microplastic strain accumulated per cycle and the influence of the evolving micro-kinematic resistance. Nevertheless, the plastic loops remain finite even at low amplitudes. Thus, microplastic dissipation decreases continuously with stress amplitude without vanishing below a distinct threshold. This behavior is consistent with the absence of a well-defined fatigue limit in many FCC metals and provides a mechanistic basis for HCF life prediction. Accordingly, the threshold-free formulation predicts continued entropy accumulation and eventual failure at any nonzero stress amplitude. Apparent fatigue limits arising from material-specific arrest or saturation mechanisms remain outside the present model.

Fig. 8 presents the simulated evolution of the active micro-defect fraction $f_v$ and micro-kinematic hardening modulus $h$ with cycle count $N$ at different stress amplitudes. Both variables are coupled to the TSI with $a_{\mathrm{fv}} = a_h = 1$. Although their dependence on $\phi$ is linear, their cycle-dependent evolution remains nonlinear because $\phi$ evolves through cumulative entropy production.

The active micro-defect fraction increases monotonically from $f_{v,0}$ toward $f_{\mathrm{sat}}$, while $h$ decreases from $h_0$ toward $h_{\mathrm{sat}}$. Both histories exhibit an S-shaped transition, with slow initial evolution, intermediate acceleration, and saturation near failure. The increase in $f_v$ represents the broadening and multiplication of active microplastic regions, whereas the decrease in $h$ reflects the loss of defect-scale kinematic resistance associated with cyclic softening. Decreasing the stress amplitude shifts both transitions to larger cycle counts. Lower amplitudes produce less microplastic dissipation per cycle, resulting in slower entropy accumulation, delayed TSI evolution, and longer fatigue life.

Fig. 9 shows the cumulative volumetric entropy production with cycle count on a logarithmic scale for different stress amplitudes. Entropy increases monotonically toward a common terminal value at failure, commonly referred to as the fracture fatigue entropy (FFE). In the present framework, this value is inferred from the entropy-TSI relation in Eq. (3) after the material parameters and $\phi_{\mathrm{cr}}$ are specified. Fig. 10 presents the corresponding TSI histories, with the predicted

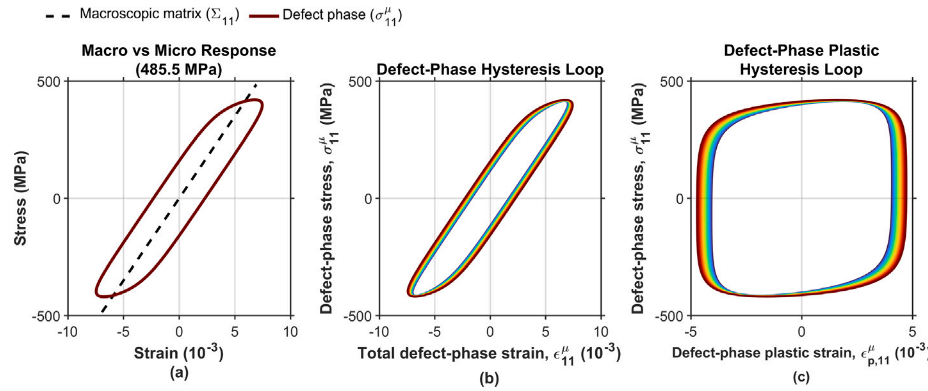


**Fig. 3.** Simulated cyclic response at 485.5 MPa. Subplots (a)–(c) show the macroscopic and micro-stress responses, the total defect-phase loop, and the micro-stress-microplastic-strain loop. The blue-to-red sequence contains 21 equally spaced TSI states from $\phi = 0$ to 0.98 and resolves the continuous change in loop shape.

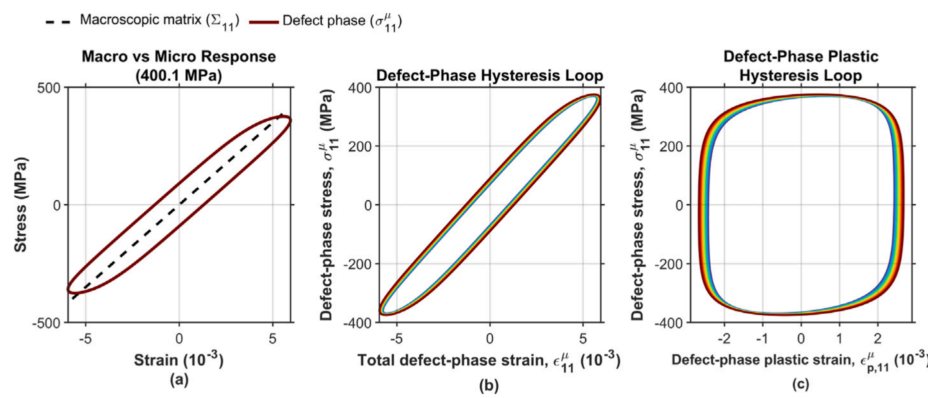


**Fig. 4.** Simulated cyclic response at 400.1 MPa. The defect-scale loop narrows relative to the 485.5 MPa case.

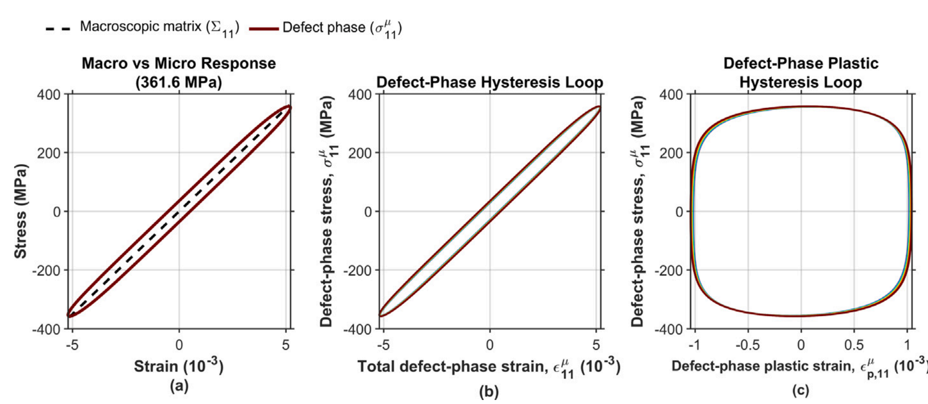


**Fig. 5.** Simulated cyclic response at 361.6 MPa. Compared with Fig. 4, the total defect-phase hysteresis loop further narrows.

fatigue life $N_f$ defined as the cycle count at which $\phi$ reaches $\phi_{\mathrm{cr}}$. Higher stress amplitudes accelerate entropy accumulation and TSI evolution, resulting in shorter fatigue lives.

The fatigue lives obtained from the TSI histories in Fig. 10 form the discrete UMT predictions shown in Fig. 11, which also compares them with Basquin and Stromeyer relations fitted to the experimental failures. Their accuracy is summarized in Table 5. In leave-one-out cross-validation, each failure point is withheld, the empirical relation is refitted to the remaining six points, and the withheld predictions are combined to calculate the error statistics. The increased error reflects the dependence of empirical relations on the calibration data. By contrast, UMT uses a fixed literature-based parameter set and prescribed evolution laws without fitting individual S–N points. Therefore, withholding one failure point leaves its predictions unchanged. Its principal advantage lies in mechanism-based forward prediction and the simultaneous description of defect-scale hysteresis, entropy accumulation, microstructural evolution, and fatigue life. Application to other materials requires their corresponding physical parameters.

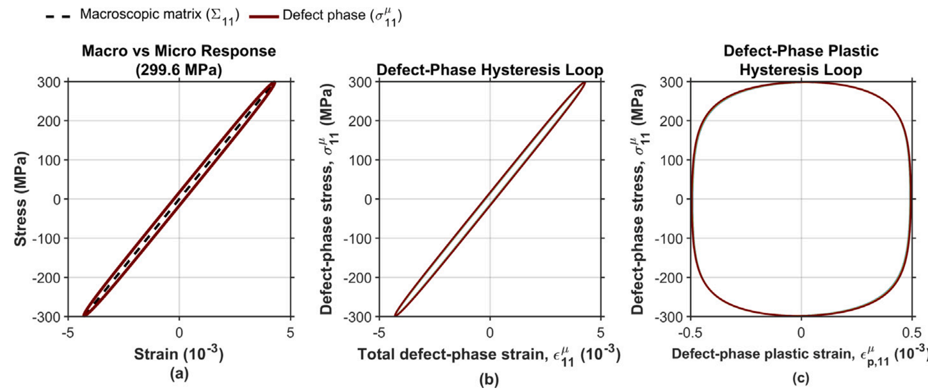


**Fig. 6.** Simulated cyclic response at 299.6 MPa. Compared with Fig. 5, the defect-phase response becomes closer to the global elastic matrix response.

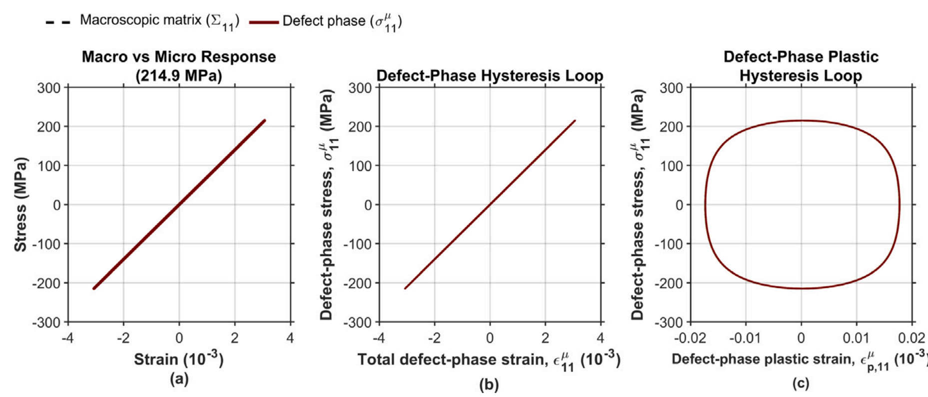


**Fig. 7.** Simulated cyclic response at 214.9 MPa. A finite but small defect-scale dissipation remains.

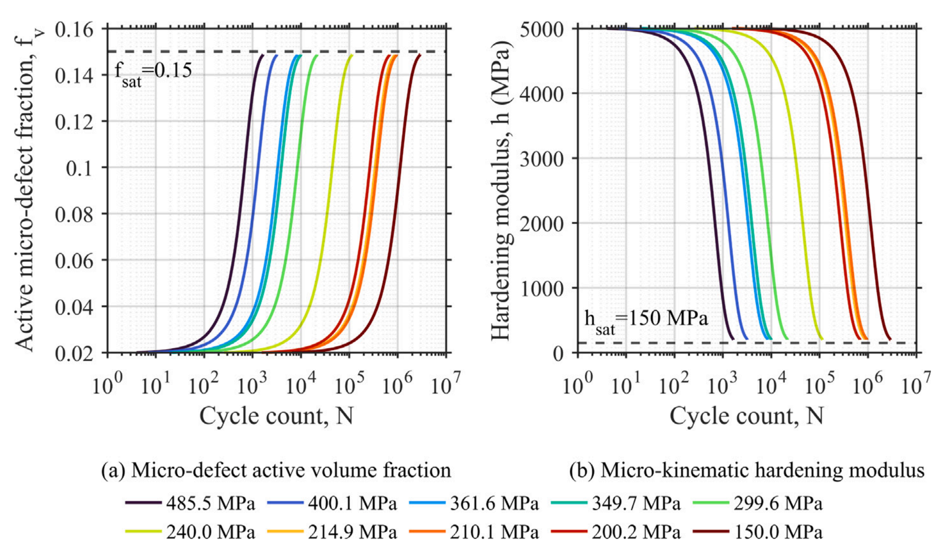


**Fig. 8.** Simulated evolution of (a) the active micro-defect fraction $f_v$ and (b) the micro-kinematic hardening modulus $h$ under the exact amplitude/frequency pairs in Table 3. Dashed horizontal lines mark the prescribed upper bound $f_{\text{sat}} = 0.15$ and lower bound $h_{\text{sat}} = 150$ MPa.

Fig. 12 presents the specimen-by-specimen comparison between the predicted and experimental fatigue lives. For the seven smooth cylindrical dog-bone specimen failures, the logarithmic root-mean-square error (log-RMSE) is 0.129 decades, the geometric mean of the predicted-to-experimental life ratios is 1.071, and all predictions lie within the factor-of-two and factor-of-three agreement bands.

### *4.2. Constant-amplitude fatigue simulations and transient local response at different stress ratios*

To assess the numerical capability of the model beyond fully reversed loading, simulations combined $R = -1$, $-0.5$, 0, and 0.3 with $\Sigma_{\max} = 320$, 360, 400, 440, and 480 MPa, yielding 20 constant-amplitude cases at $T = 298$ K and $f = 10$ Hz. The corresponding mean

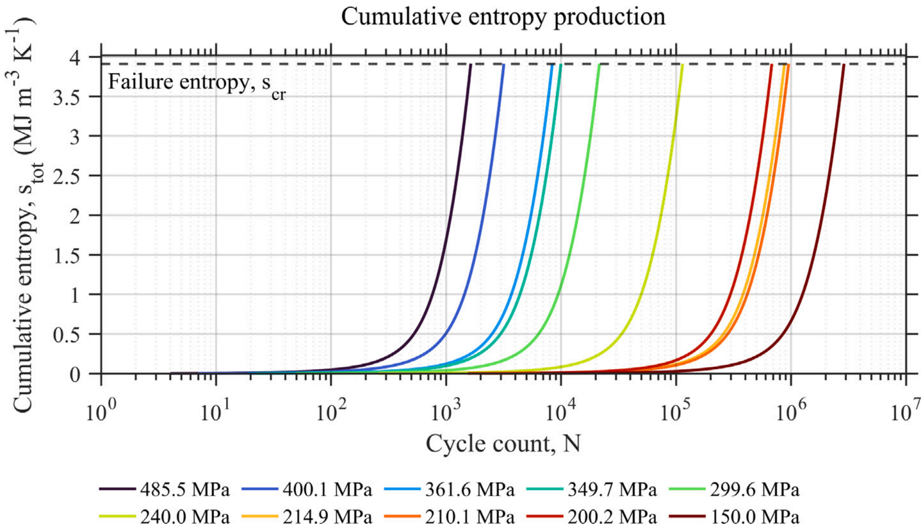


**Fig. 9.** Simulated evolution of cumulative volumetric entropy production versus cycle count for different prescribed stress amplitudes. In the present framework, the entropy threshold at failure is not imposed directly from experiment, but emerges numerically once the material parameters and the critical TSI value are specified.

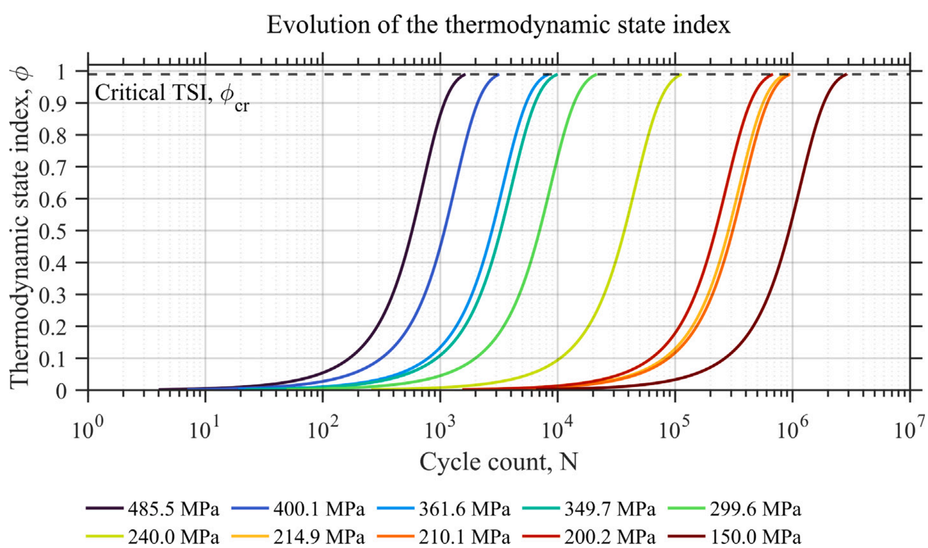


**Fig. 10.** Simulated TSI histories for different prescribed stress amplitudes; the first integer cycle reaching $\phi_{cr} = 0.99$ defines the predicted life.

**Table 5**
Accuracy of the UMT predictions and empirical S–N baselines for the seven experimental failures.

| Method | log-RMSE (decades) | Factor 2 (%) | Factor 3 (%) |
|---|---|---|---|
| UMT (fixed parameter set) | 0.129 | 100 | 100 |
| Basquin (all data) | 0.121 | 100 | 100 |
| Stromeyer (all data) | 0.092 | 100 | 100 |
| Basquin (leave-one-out) | 0.205 | 85.7 | 100 |
| Stromeyer (leave-one-out) | 0.192 | 85.7 | 100 |

stresses and stress amplitudes were determined from the relations in Section 3.1, and the cylindrical benchmark parameter set was retained without further adjustment.

The accelerated block scheme in Section 3.1 replaces the initial transient response with stabilized-cycle work during block integration. To assess this approximation and examine transient local ratcheting followed by shakedown under nonzero mean stress, per-cycle resolved calculations were initiated from $\epsilon_p^{\mu} = \mathbf{0}$ for all four stress ratios at the representative $\Sigma_{\max} = 400$ MPa.

Each cycle was integrated to stabilization while accumulating microplastic work and entropy production. The transition-work difference between the two schemes was divided by the accelerated block scheme's stabilized work per cycle to obtain the equivalent life correction, whose magnitude relative to the predicted fatigue life defines the relative correction. Fig. 13 shows that the $R = -1$, $-0.5$, 0, and 0.3 cases stabilized after 21, 79, 236, and 418 cycles, respectively. The active micro-defect fraction and micro-kinematic hardening modulus were fixed at their initial values to isolate the transient response. For all cases, the relative correction remained below $9.7 \times 10^{-5}$ within the present formulation.

The downward-right translation in Figs. 13(b)–(d) follows from the axial localization relation

$$\sigma_{11}^{\mu} = \Sigma_{11} - K_{\mathrm{loc}}\epsilon_{p,11}^{\mu}, \qquad K_{\mathrm{loc}} = 2\mu(1-\beta)(1-f_v) > 0. \tag{29}$$

Under tensile mean stress, positive microplastic strain accumulation shifts the loop rightward, while, at a fixed macroscopic stress, the term $-K_{\mathrm{loc}}\epsilon_{p,11}^{\mu}$ lowers the micro-stress and produces the downward shift. Within the current linear localization and kinematic-hardening framework, this transient represents local tensile microplastic accumulation

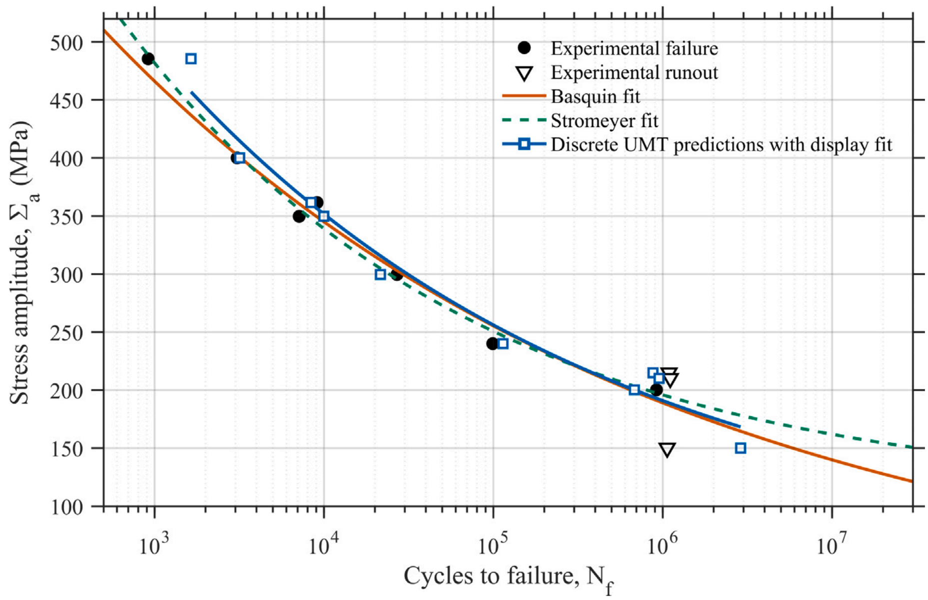


**Fig. 11.** UMT predictions, experimental failures and runouts, and Basquin and Stromeyer fits to the experimental failure data. The smooth curve through the discrete UMT points is included only as a visual guide and is not used to calculate fatigue life.

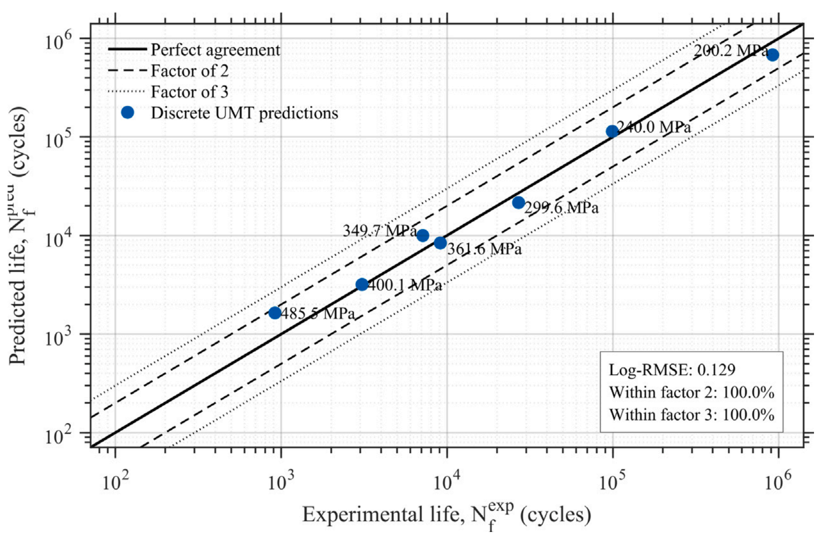


**Fig. 12.** Predicted-versus-experimental fatigue life comparison for the proposed UMT model. The solid diagonal line denotes perfect agreement, and the dashed and dotted lines indicate the factor-of-2 and factor-of-3 agreement bands, respectively.

and stress relaxation followed by shakedown. Such rapid stabilization can be plausible in HCF because microplastic deformation remains confined to a small active volume while the matrix remains macroscopically elastic. If experiments reveal progressive local ratcheting, slow mean-strain relaxation, nonlinear backstress recovery, or appreciable crack-opening or closure effects in the tested material system, additional constitutive or damage mechanisms would be required; these behaviors define the present model limitations.

Fig. 14 presents the predicted $\Sigma_{max}$–life responses. At fixed $\Sigma_{max}$, increasing $R$ reduces $\Sigma_a$; within the present formulation, this reduction dominates the modeled mean-stress response and increases the predicted life. The same parameter set was retained for all stress ratios without further adjustment. These results demonstrate numerical capability beyond $R = -1$. Broader validation requires independent fatigue experiments spanning multiple stress ratios, while improved quantitative prediction may require additional mean-stress-sensitive dissipation mechanisms. The following smooth flat dog-bone specimen assessment provides a limited evaluation against $R \approx 0$ fatigue data.

### *4.3. Fatigue-life simulation of smooth flat dog-bone specimens at different stress ratios*

Zhao and Jiang [89] also report room-temperature HCF data for smooth flat dog-bone specimens oriented at 0° and 90° to the plate rolling direction and tested at $R = -1$ and $R \approx 0$. Although the nominal alloy and temper are unchanged, the plate and cylindrical tests constitute separate specimen series whose effective localized-slip responses may differ because of specimen form, texture, surface initiation, and local constraint. The parameters $\Delta F_0$ and $V_{act}$ were therefore adopted within literature-reported ranges for the plate baseline simulations at $R = -1$, giving 0.5923 eV and $5.5b^3$, while all other parameters were retained. These values differ from the cylindrical baseline by only 5.5% and 10.0%, respectively. No orientation-dependent adjustment was introduced. The same plate parameter set was applied to both orientations and subsequently retained for prediction of the $R \approx 0$ fatigue lives.

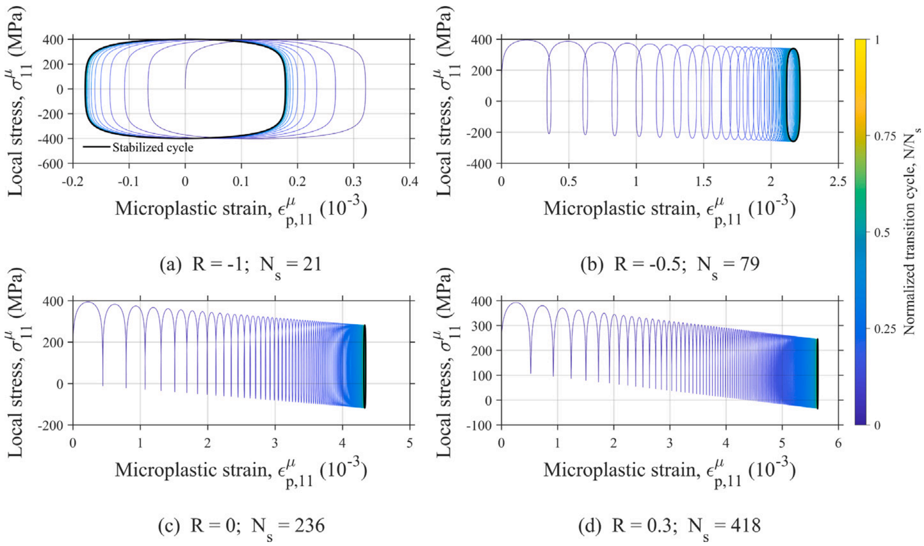


**Fig. 13.** Per-cycle resolved transition of the micro-stress-microplastic-strain loops from the virgin state to stabilization at $\Sigma_{\max} = 400$ MPa. Each cycle is colored by the normalized transition progress $\eta_N = N/N_s$, where $N_s$ is the number of cycles required to reach the periodic state for each stress ratio. The stabilized loop is outlined in black.

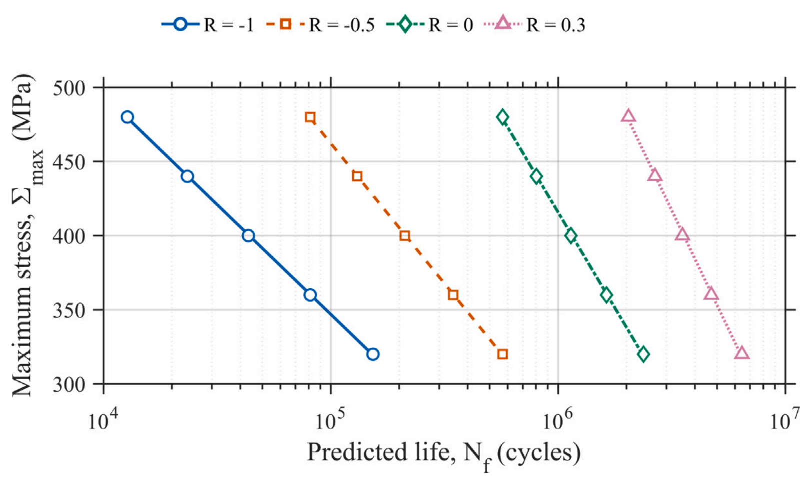


**Fig. 14.** Constant-amplitude AA7075-T651 predictions at four stress ratios using the unchanged cylindrical benchmark parameter set. Markers denote discrete UMT predictions, and lines are least-squares fits of $\Sigma_{\max} = b_0 + b_1 \log_{10} N_f$.

Fig. 15 compares the experiments with the plate $R = -1$ baseline simulation and the $R \approx 0$ prediction. Straight lines are least-squares S–N fits to the respective discrete data and are included only for visualization. For the 39 $R = -1$ failures, the log-RMSE is 0.255 decades, the geometric mean of the predicted-to-experimental life ratios is 1.01, and 97.4% of predictions lie within a factor of three. For the 15 $R \approx 0$ failures within the nominally elastic HCF range considered here, the corresponding values are 0.461 decades, 2.40, and 46.7%, with all predictions within a factor of five. Table 6 summarizes these metrics. For the four runouts, the predicted lives were shorter than the reported test durations.

For the $R \approx 0$ failure data, predictions generally overestimate fatigue life, indicating insufficient damage accumulation under tension–tension loading in the present formulation. The bias is smaller for several of the lowest-amplitude cases. The residual bias and runout discrepancies suggest that tensile-stress-assisted damage, surface-crack initiation, and reduced crack closure may contribute to fatigue degradation beyond the localized microplastic work represented here. These results define the model's current applicability limits and motivate independent fatigue tests spanning multiple stress ratios, together with additional mean- or maximum-stress-sensitive dissipation mechanisms.

**Table 6**
Fatigue-life prediction metrics for failures of smooth flat dog-bone specimens at $R = -1$ and $R \approx 0$. The geometric mean life ratio is calculated from $N_f^{\mathrm{pred}}/N_f^{\exp}$.

| Stage | $n$ | log-RMSE (decades) | Geometric mean life ratio | Within ×2 | Within ×3 |
|---|---|---|---|---|---|
| $R = -1$ baseline simulation | 39 | 0.255 | 1.01 | 76.9% | 97.4% |
| $R \approx 0$ prediction | 15 | 0.461 | 2.40 | 40.0% | 46.7% |

### 4.4. Sensitivity study on the numerical results

Because several parameters adopted for the benchmark simulation in Section 4.1 were not directly measured, a targeted sensitivity study was performed to examine their influence on the predicted fatigue response. Each parameter group was varied individually from its benchmark value while all others remained fixed. The investigated groups included $\phi_{\mathrm{cr}}$, $a_{\mathrm{fv}}$, $a_h$, $(f_{v,0}, f_{\mathrm{sat}})$, $(h_0, h_{\mathrm{sat}})$, $\Delta F_0$, and $V_{\mathrm{act}}$. For each variation, the numerical procedure in Section 3.1 was repeated over the prescribed stress amplitudes, and changes in predicted life and state-

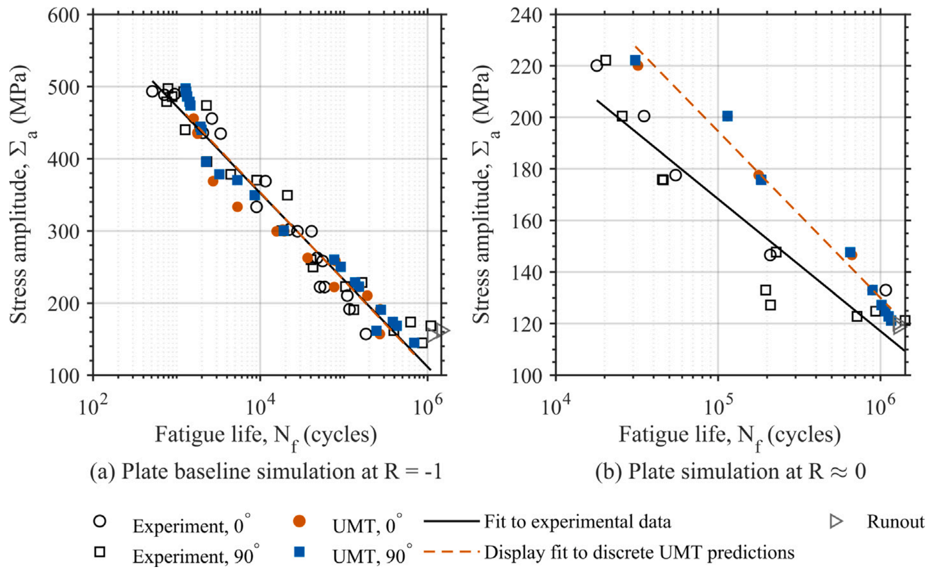


**Fig. 15.** Experimental and predicted S–N responses of smooth flat dog-bone specimens oriented at 0° and 90° to the rolling direction: (a) $R = -1$ baseline and (b) $R \approx 0$ prediction. No systematic orientation dependence is evident within the experimental scatter; both orientations are therefore evaluated using a common parameter set as combined comparison data.

**Table 7**
Test values adopted in the sensitivity study for the AA7075-T651 benchmark problem.

| Parameter group | Benchmark | Sensitivity values |
|---|---|---|
| Critical TSI at failure, $\phi_{cr}$ | 0.99 | 0.97, 0.95 |
| Defect-fraction exponent, $a_{fv}$ | 1.0 | 0.5, 2.0 |
| Hardening evolution exponent, $a_h$ | 1.0 | 0.5, 2.0 |
| Active micro-defect bounds, ($f_{v,0}$, $f_{sat}$) | (0.02, 0.15) | (0.002, 0.15), (0.02, 0.25) |
| Micro-kinematic hardening moduli, ($h_0$, $h_{sat}$) [MPa] | (5000, 150) | (5000, 50), (7500, 150) |
| Activation energy, $\Delta F_0$ [eV] | 0.627 | 0.55, 0.75 |
| Activation volume, $V_{act}$ [$b^3$] | 5 | 7.5, 10 |

variable evolution were compared with the benchmark response. Table 7 lists the corresponding test values.

Fig. 16 shows the influence of the critical TSI value, $\phi_{cr}$, on the predicted S–N response. Reducing $\phi_{cr}$ from 0.99 to 0.97 and 0.95 slightly shortens the predicted lives because less cumulative entropy is required to satisfy the failure condition. The curves remain nearly parallel to the benchmark response, indicating that $\phi_{cr}$ primarily changes the failure threshold rather than the S–N slope. Its effect is therefore systematic but relatively small over the tested range. This moderate sensitivity follows from the exponential TSI relation, $\phi = 1 - \exp(-A_\phi s_{tot})$, for which small reductions near $\phi_{cr} = 0.99$ gradually decrease the required failure entropy. A value closer to unity, such as $\phi_{cr} = 0.999$, would increase the entropy threshold more substantially and produce a larger change in predicted life.

Fig. 17 compares the sensitivity to the microstructural evolution parameters and their bounds. The active micro-defect fraction bounds have the greatest influence because $f_v$ directly scales the bulk-averaged microplastic dissipation and entropy production per cycle. Increasing $f_v$ enlarges the effective dissipating volume and accelerates damage accumulation, whereas reducing it delays entropy accumulation and extends fatigue life. The exponent $a_{fv}$ has a weaker effect, indicating greater sensitivity to the admissible range of active microplastic regions than to their transition shape. Variations in $a_h$ and the bounds of $h$ produce only minor changes. For the present benchmark, fatigue life is therefore governed more strongly by the amount of active microplastic material than by the detailed evolution of the micro-kinematic hardening modulus.

Fig. 18 shows that the thermally activated parameters exert the strongest influence on the predicted S–N response. The activation energy $\Delta F_0$ is particularly influential. Increasing $\Delta F_0$ to 0.75 eV shifts the predicted fatigue lives substantially to the right, whereas reducing it to 0.55 eV shifts the response strongly to the left. This occurs because $\Delta F_0$ enters the Eyring-type flow rule through the exponential factor $\exp(-\Delta F_0/k_B T)$. Therefore, even a moderate change in $\Delta F_0$ can significantly alter the microplastic slip rate, the dissipated energy per cycle, and the rate of entropy accumulation. The activation volume $V_{act}$ also has a pronounced effect because it controls the stress sensitivity of the thermally activated slip term through $\sinh(V_{act}\tau_{eff}/k_B T)$. Increasing $V_{act}$ therefore amplifies the response to the effective resolved shear stress, leading to faster microplastic accumulation and shorter predicted fatigue lives.

To further quantify the relative influence of each parameter, Fig. 19 summarizes the global sensitivity using the mean absolute difference in logarithmic fatigue life, $\mathrm{Mean}|\Delta \log_{10}(N_f)|$, relative to the benchmark case. This metric is adopted because fatigue life varies over several orders of magnitude; therefore, differences in $\log_{10}(N_f)$ provide a more meaningful measure of relative life shifts than direct cycle-count differences. For reference, $|\Delta \log_{10}(N_f)| = 0.3$ corresponds approximately to a factor-of-two difference in fatigue life, while $|\Delta \log_{10}(N_f)| = 1$ corresponds to one order-of-magnitude difference.

The results confirm that the thermally activated parameters dominate the model sensitivity over the tested ranges. Relative to the benchmark case, decreasing and increasing $\Delta F_0$ to 0.55 and 0.75 eV

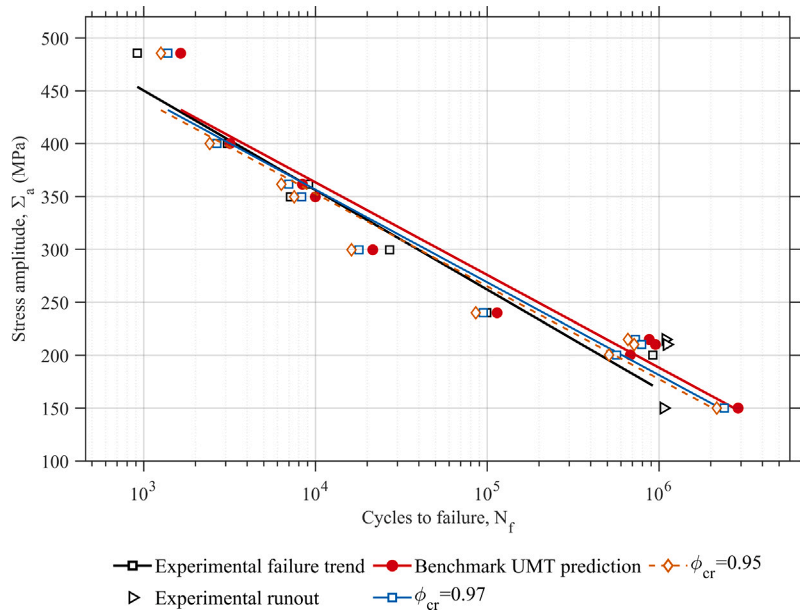


**Fig. 16.** Sensitivity of the predicted S–N response to the critical TSI value $\phi_{cr}$. Experimental failures and the runout are shown for reference. For every simulated case, markers denote discrete predictions and the corresponding line is a least-squares S–N display fit.

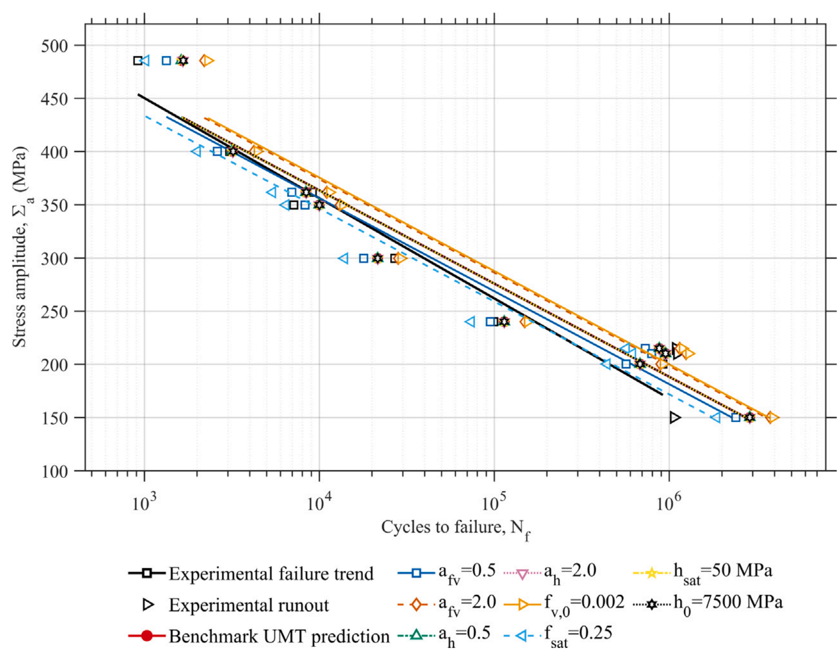


**Fig. 17.** Sensitivity to the active micro-defect fraction and micro-kinematic hardening evolution exponents and endpoint bounds. Experimental failures and the runout are shown for reference. Markers denote discrete calculations and the corresponding lines are least-squares display fits.

produce Mean$|\Delta \log_{10}(N_f)|$ values of 0.86 and 2.00, respectively. This pronounced sensitivity arises from the exponential dependence of the Eyring flow rate on $\Delta F_0$. Increasing $V_{act}$ from $5b^3$ to $7.5b^3$ and $10b^3$ gives corresponding values of 0.46 and 0.75. The active micro-defect fraction bounds are the next most influential parameters, with values of 0.14–0.19, while the effects of $\phi_{cr}$ are 0.08–0.12 and those of the micro-kinematic hardening parameters remain below 0.002.

### *4.5. Microstructural parameter evolution laws and coupled parameter sensitivity*

Fig. 20 compares the power, normalized-exponential ($k = 4$), and smoothstep functions used in Eqs. (13) and (15). Relative to the power law, the normalized-exponential and smoothstep forms give Mean$|\Delta \log_{10}(N_f)|$ values of 0.108 and 0.019, respectively. Reversing $(h_0, h_{sat})$ from $(5000, 150)$ to $(150, 5000)$ MPa changes the predicted life at 299.6 MPa from 21,550 to 21,570 cycles, corresponding to $|\Delta \log_{10}(N_f)| < 0.001$. This calculation demonstrates that the generalized evolution relation can represent an increasing micro-kinematic hardening modulus, although validation of this behavior requires cyclic-hardening data.

The coupled sensitivity of the parameter pairs $(C_{RT}, V_{act})$, $(f_{v,0}, f_{sat})$, and $(h_0, h_{sat})$ was evaluated using $19 \times 19$ parameter grids, comprising 19 sampled values for each parameter and 361 combinations per pair, at $\Sigma_a$ = 485.5, 299.6, and 200.2 MPa. At fixed temperature, $\dot{\gamma}_0$ and $\Delta F_0$ enter the Eyring law through the combined kinetic factor $C_{RT}$ =

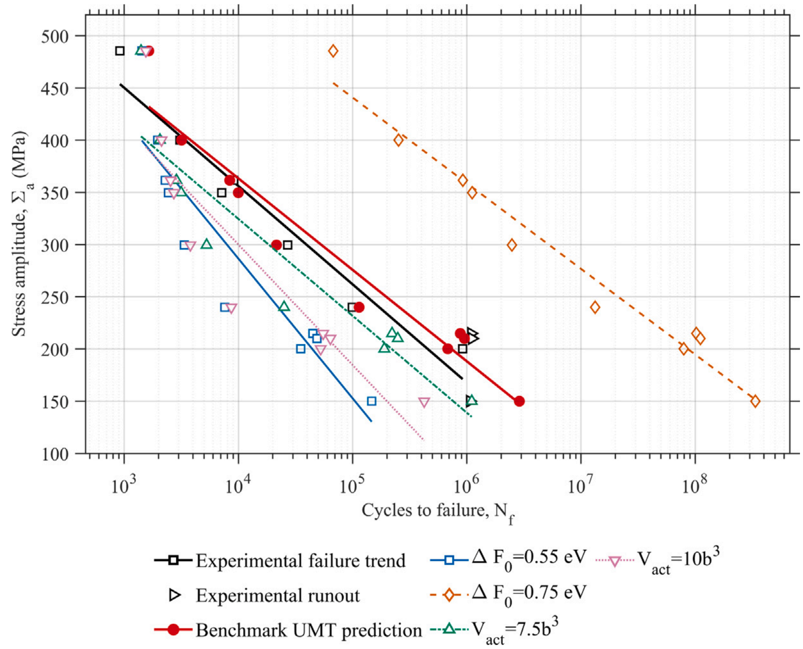


**Fig. 18.** Sensitivity to the thermally activated parameters $\Delta F_0$ and $V_{\mathrm{act}}$. Experimental failures and the runout are shown for reference. Markers denote discrete predictions and the corresponding lines are least-squares display fits.

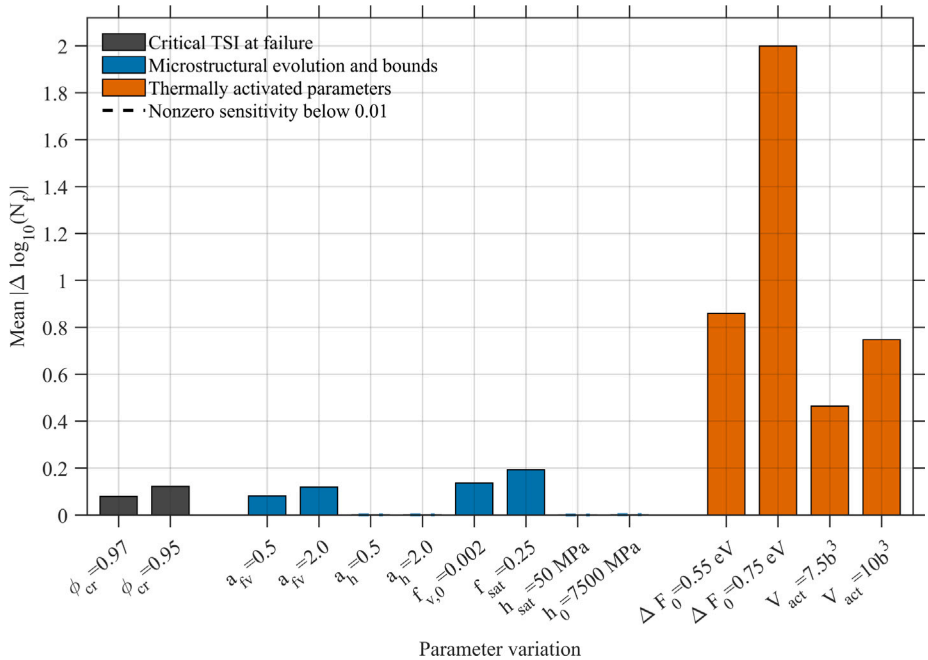


**Fig. 19.** Global sensitivity of the predicted fatigue life to model parameters, quantified by the mean absolute logarithmic life difference relative to the benchmark case.

$\dot{\gamma}_0 \exp[-\Delta F_0/(k_B T)]$. For two parameters sampled at values $x_i$ and $y_j$, let $Z_{ij} = \log_{10} N_f(x_i, y_j)$. Their nonadditivity residual is defined as

$$I_{ij} = Z_{ij} - \overline{Z}_{i\cdot} - \overline{Z}_{\cdot j} + \overline{Z}_{\cdot\cdot}, \tag{30}$$

where $\overline{Z}_{i\cdot}$, $\overline{Z}_{\cdot j}$, and $\overline{Z}_{\cdot\cdot}$ are the row, column, and overall grid means, respectively. A value of $I_{ij} = 0$ indicates additive effects on the logarithmic life scale, while a nonzero value measures parameter interaction. Figs. 21–23 use separate symmetric color scales for $I_{ij}$ because the interaction magnitudes differ substantially; black contours show $\log_{10} N_f$.

The kinetic pair $C_{\mathrm{RT}}$–$V_{\mathrm{act}}$ produces the largest life variation, spanning 1.03–1.65 decades depending on stress amplitude, and the strongest interaction, with $\max|I_{ij}| = 0.182$ at $\Sigma_a = 485.5$ MPa. The $f_{v,0}$–$f_{\mathrm{sat}}$ pair spans 0.38–0.42 decades, with $\max|I_{ij}| < 0.004$, whereas the $h_0$–$h_{\mathrm{sat}}$ pair spans at most 0.014 decades, with $\max|I_{ij}| < 1.67 \times 10^{-4}$. Thus, the coupled sensitivity is concentrated primarily in the kinetic

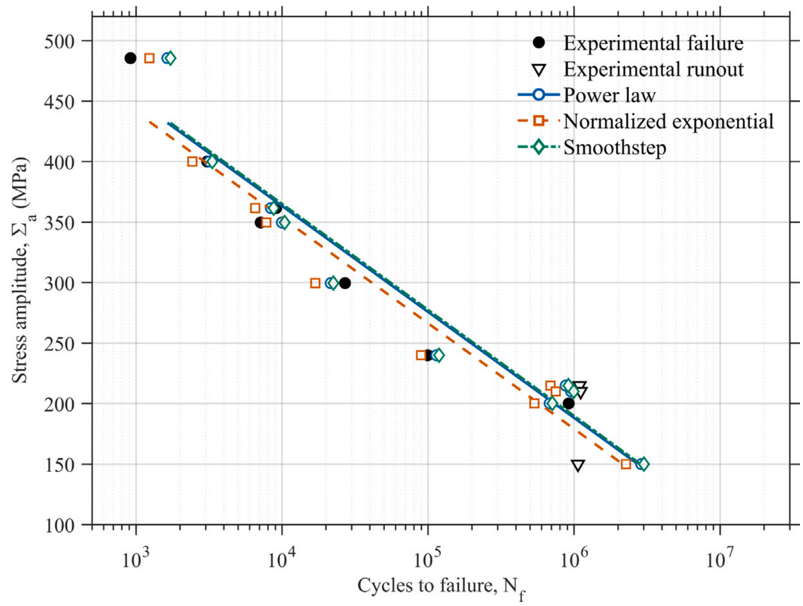


**Fig. 20.** S–N predictions using three bounded microstructural parameter evolution laws with common endpoints. Experimental failures and the runout are retained for reference. Markers denote discrete predictions and the corresponding lines are least-squares display fits.

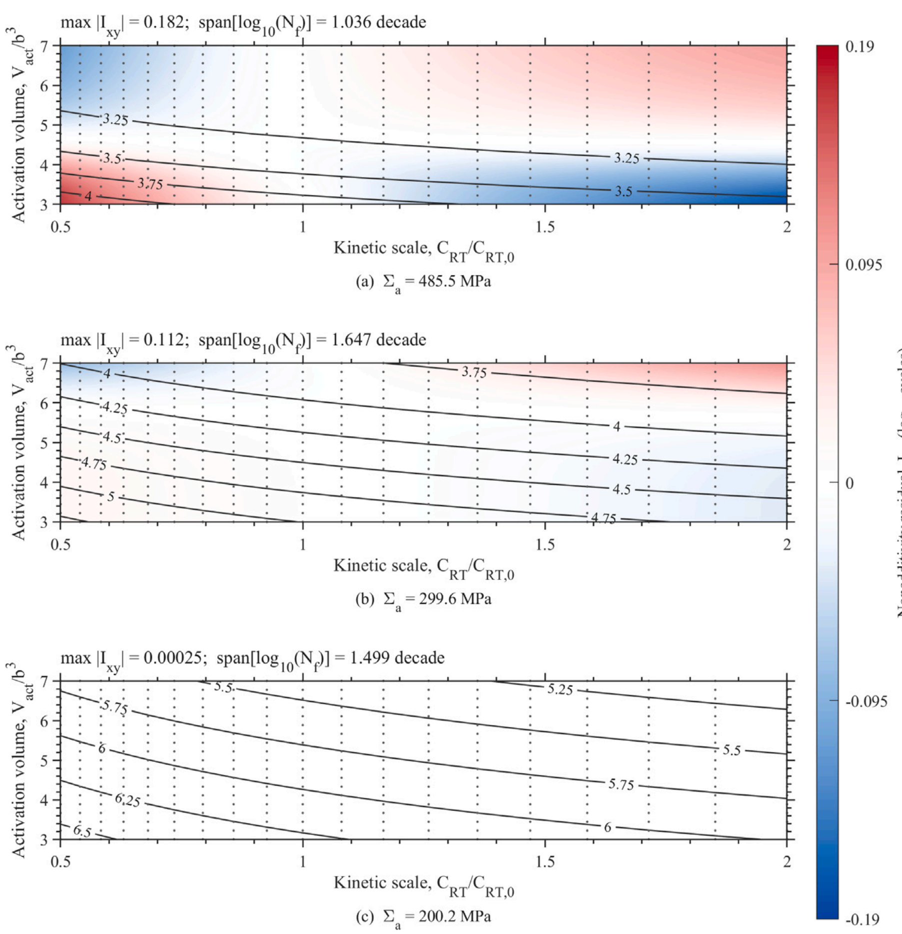


**Fig. 21.** Coupled sensitivity of $C_{\mathrm{RT}}$ and $V_{\mathrm{act}}$ at three stress amplitudes. Colors show $I_{ij}$, black contours show $\log_{10} N_f$, and gray markers indicate the sampled combinations.

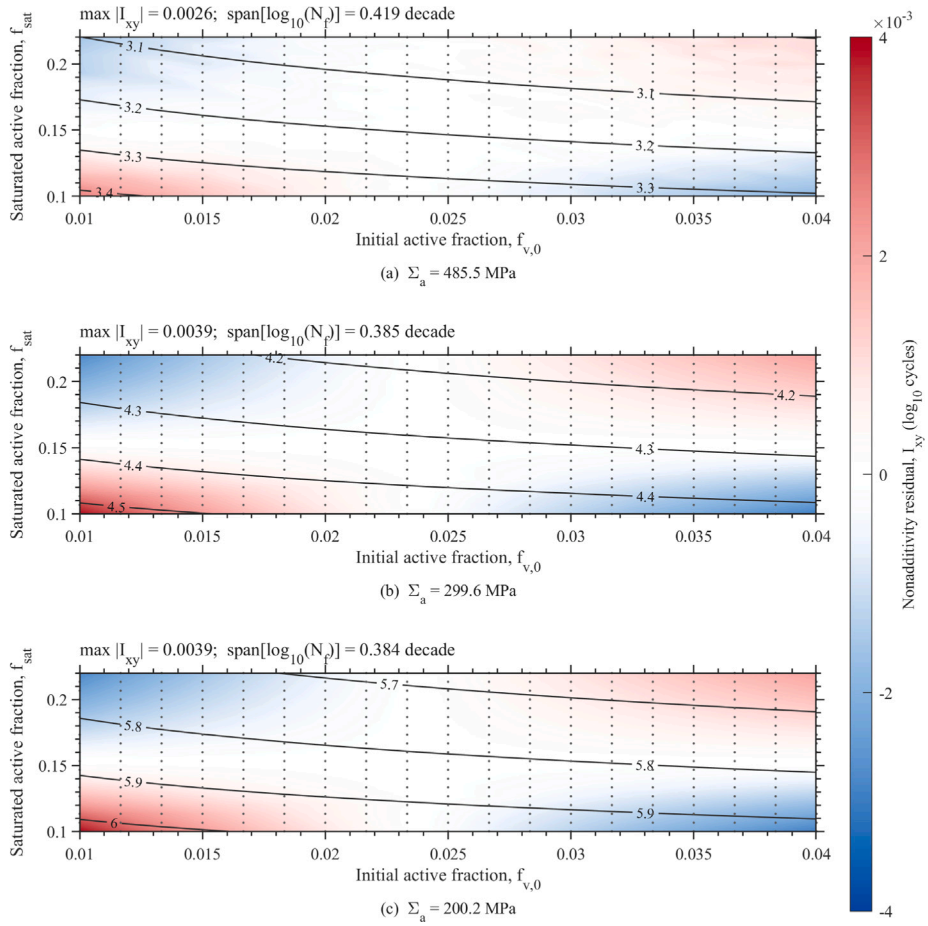


**Fig. 22.** Coupled sensitivity of $f_{v,0}$ and $f_{sat}$ at three stress amplitudes. Colors show $I_{ij}$, black contours show $\log_{10} N_f$, and gray markers indicate the sampled combinations.

parameters, emphasizing the need for their independent experimental characterization.

## 5. Conclusions and limitations

A UMT-based HCF model was developed for FCC metals and assessed using AA7075-T651 as a benchmark. The TSI evolves through cumulative entropy production and serves as the degradation variable. Within the two-scale framework, the macroscopic response remains nominally elastic while irreversible dissipation develops in localized microplastic zones. The work-conjugate effective force ensures non-negative microplastic-flow dissipation consistent with the second law of thermodynamics. Compared with earlier BCC-based formulations, the present FCC model removes the explicit micro-yielding threshold and introduces thermally activated flow to describe gradual cyclic irreversibility that can occur even at low stress amplitudes. Bounded microstructural parameter evolution laws further connect entropy accumulation with the active micro-defect fraction and micro-kinematic hardening modulus.

The model was assessed against fully reversed fatigue data for smooth cylindrical dog-bone specimens made of AA7075-T651. The predicted S–N response follows the experimental trend with a log-RMSE of 0.129 decades, and all seven failure predictions lie within a factor of two. The UMT model also links crystallographically motivated thermally activated slip, localized hysteresis and dissipation, entropy production, microstructural evolution, and fatigue life, providing physical-state information beyond conventional empirical S–N relations. Additional simulations for $R = -1$, $-0.5$, 0, and 0.3 at five fixed maximum stresses assessed the numerical capability beyond fully reversed fatigue. Per-cycle resolved calculations showed transient local ratcheting followed by rapid shakedown within the current linear localization and hardening formulation. In the smooth flat dog-bone specimen assessment, the literature-based plate parameter set adopted for the $R = -1$ baseline was retained without further adjustment for prediction at $R \approx 0$, giving a geometric mean of the predicted-to-experimental life ratios of 2.40, with 46.7% and 100% of predictions within factors of three and five, respectively. The remaining difference between the predicted and experimental $R \approx 0$ lives indicates limited quantitative accuracy under tension–tension loading.

The sensitivity study showed comparatively small effects from the critical TSI and micro-kinematic hardening parameters, while the active micro-defect fraction bounds were more influential because they control the dissipating volume. The strongest sensitivity arose from $\Delta F_0$ and $V_{act}$, which govern the rate of thermally activated slip. The tested alternative bounded microstructural parameter evolution laws produced modest shifts in predicted fatigue life while preserving the overall S–N response, with substantially smaller effects than the thermally activated kinetic parameters. The coupled analysis identified the strongest interaction for $C_{RT}$–$V_{act}$; the active micro-defect fraction effects were moderate and nearly additive, while interaction between the micro-kinematic hardening endpoints was negligible.

Nevertheless, the primary validation remains limited to room-temperature, fully reversed HCF of FCC aluminum alloy, while the secondary plate assessment at $R \approx 0$ still overpredicts fatigue life. The present model is intended for conventional-frequency HCF and does not account for rapid specimen self-heating that may occur during ultrasonic fatigue at frequencies near 20 kHz or above. Specimen heating changes the combined influence of $\Delta F_0$ and $V_{act}$ on thermally

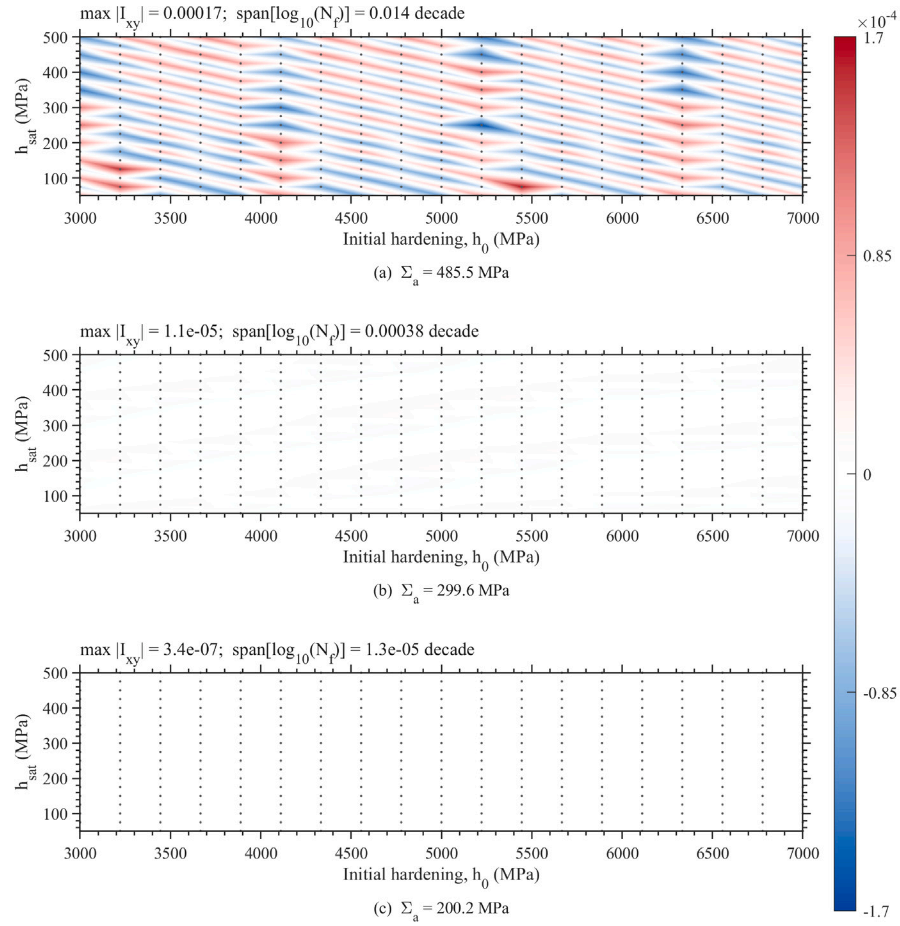


**Fig. 23.** Coupled sensitivity of $h_0$ and $h_{\text{sat}}$ at three stress amplitudes. Colors show $I_{ij}$, black contours show $\log_{10} N_f$, and gray markers indicate the sampled combinations.

activated slip. The present room-temperature data cannot establish this dependence, so temperature-transfer capability remains unvalidated. Under nonzero mean stress, the linear localization and hardening relations promote rapid local shakedown. This response can be physically plausible in HCF because microplastic deformation remains confined to small active zones while the macroscopic matrix remains nominally elastic. If HCF experiments nevertheless reveal progressive local ratcheting, slow local mean-strain relaxation, nonlinear backstress recovery, tensile-stress-assisted damage, or appreciable crack-opening and closure effects, additional constitutive or entropy production mechanisms would be required. Finally, the proposed model also does not resolve specimen scatter, rolling-direction texture effects, individual manufacturing-defect morphology, or explicit persistent-slip-band and grain-boundary-cavity evolution.

Future work should include independently characterized fatigue datasets spanning multiple stress ratios and temperatures, cyclic tests at different loading rates, and direct measurements of microplasticity and stabilized hysteresis responses. Interrupted-test EBSD, TEM, and surface observations can support identification of the active micro-defect fraction and its evolution. Ultrasonic-fatigue applications require modeling of self-heating caused by internal friction and coupling the entropy-production model with transient thermal analysis. If persistent local ratcheting or appreciable tensile mean-stress effects are observed under HCF conditions, nonlinear kinematic-hardening and recovery relations, mean- or maximum-stress-sensitive dissipation mechanisms, and crack-opening and closure descriptions should be considered. Explicit finite-element representation of manufacturing-defect size, shape, and location can provide the corresponding micro-stress and entropy-production fields, while probabilistic formulations can address fatigue scatter and censored runouts. Sequence-dependent variable-amplitude loading requires a history-carrying cycle-by-cycle solver. Extension to additional FCC materials using independently determined physical parameters remains essential for establishing the framework's broader predictive capability.

## Declaration of competing interest

The authors declare that they have no known competing financial interests or personal relationships that could have appeared to influence the work reported in this paper.

## Acknowledgments

The author acknowledges financial support from the National Science and Technology Council (NSTC), Taiwan, under Research Project No. 115-2222-E-006-003-MY2. The computational work was carried out at the Department of Aeronautics and Astronautics, National Cheng Kung University.

## Data availability

Data will be made available on request.

## References


[1] Zhang P, Zhu Q, Chen G, Qin H, Wang C. Effect of heat treatment process on microstructure and fatigue behavior of a nickel-base superalloy. Materials 2015;8(9):6179–94.
[2] Riccius JR, Zametaev EB. HCF and LCF analysis of a generic full admission turbine blade. Aerospace 2023;10(2):154.
[3] Gao Y, Stölken J, Kumar M, Ritchie R. High-cycle fatigue of nickel-base superalloy René 104 (ME3): Interaction of microstructurally small cracks with grain boundaries of known character. Acta Mater 2007;55(9):3155–67.
[4] Kunz L, Lukáš P, Konečná R. High-cycle fatigue of Ni-base superalloy Inconel 713LC. Int J Fatigue 2010;32(6):908–13.
[5] Shridhar K, Suresh B, Kumar MM. Fatigue analysis of wing-fuselage lug section of a transport aircraft. Procedia Struct Integr 2019;14:375–83.
[6] Al-Mukhtar A. Aircraft fuselage cracking and simulation. Procedia Struct Integr 2020;28:124–31.
[7] Srivatsan T, Anand S, Sriram S, Vasudevan V. The high-cycle fatigue and fracture behavior of aluminum alloy 7055. Mater Sci Eng: A 2000;281(1–2):292–304.
[8] Coffin Jr LF. A study of the effects of cyclic thermal stresses on a ductile metal. Trans Am Soc Mech Eng 1954;76(6):931–49.
[9] Manson SS. Behavior of Materials Under Conditions of Thermal Stress, vol. 2933, National Advisory Committee for Aeronautics; 1953.
[10] Santecchia E, Hamouda A, Musharavati F, Zalnezhad E, Cabibbo M, El Mehtedi M, Spigarelli S. A review on fatigue life prediction methods for metals. Adv Mater Sci Eng 2016;2016(1):9573524.
[11] Oh B. The exponential law of endurance tests. In: Proc am soc test mater, vol. 10, 1910, p. 625–30.
[12] Zaretsky EV. A. Palmgren revisited: A basis for bearing life prediction. 1997, STLE Annual Meeting, E-10555.
[13] Miner MA. Cumulative damage in fatigue. 1945, American Society of Mechanical Engineers.
[14] Xue L. A unified expression for low cycle fatigue and extremely low cycle fatigue and its implication for monotonic loading. Int J Fatigue 2008;30(10–11):1691–8.
[15] Mesmacque G, Garcia S, Amrouche A, Rubio-Gonzalez C. Sequential law in multiaxial fatigue, a new damage indicator. Int J Fatigue 2005;27(4):461–7.
[16] Chaboche J. Continuum damage mechanics: present state and future trends. Nucl Eng Des 1987;105(1):19–33.
[17] Xiao Y-C, Li S, Gao Z. A continuum damage mechanics model for high cycle fatigue. Int J Fatigue 1998;20(7):503–8.
[18] Chow C, Wei Y. A model of continuum damage mechanics for fatigue failure. Int J Fract 1991;50(4):301–16.
[19] Batsoulas ND. Cumulative fatigue damage: CDM-based engineering rule and life prediction aspect. Steel Res Int 2016;87(12):1670–7.
[20] Zhan Z, Li H. A novel approach based on the elastoplastic fatigue damage and machine learning models for life prediction of aerospace alloy parts fabricated by additive manufacturing. Int J Fatigue 2021;145:106089.
[21] Xu Z, Yang C, Shi F, Liu W, Xu N, Hu Z, Li C, Liu K, Cao P, Wang D. Multiaxial fatigue life assessment of large welded flange shafts: A continuum damage mechanics approach. Materials 2025;18(24):5528.
[22] Wang Q, Pidaparti R, Palakal M. Comparative study of corrosion-fatigue in aircraft materials. AIAA J 2001;39(2):325–30.
[23] Zhao T, Liu Z, Du C, Liu C, Xu X, Li X. Modeling for corrosion fatigue crack initiation life based on corrosion kinetics and equivalent initial flaw size theory. Corros Sci 2018;142:277–83.
[24] Larrosa N, Akid R, Ainsworth R. Corrosion-fatigue: a review of damage tolerance models. Int Mater Rev 2018;63(5):283–308.
[25] Traidia A, Chatzidouros E, Jouiad M. Review of hydrogen-assisted cracking models for application to service lifetime prediction and challenges in the oil and gas industry. Corros Rev 2018;36(4):323–47.
[26] Golahmar A, Kristensen PK, Niordson CF, Martínez-Pañeda E. A phase field model for hydrogen-assisted fatigue. Int J Fatigue 2022;154:106521.
[27] Nazar S, Proverbio E. Modeling of hydrogen-assisted fatigue crack growth in carbon steel pipelines. Int J Hydrog Energy 2025;138:548–58.
[28] Rodríguez-Reyes VI, Abúndez-Pliego A, Petatan-Bahena KE, Miranda-Acatitlan KR, Colín-Ocampo J, Blanco-Ortega A. Comparative evaluation of fatigue life estimation under variable amplitude loading through damage models based on entropy. Fatigue Fract Eng Mater Struct 2024;47(5):1584–601.
[29] Zajkani A, Khonsari M. A unified thermomechanically-consistent framework for fatigue failure entropy. Mech Mater 2025;207:105379.
[30] Koottaparambil L, Khonsari MM. Entropy-based unified theory of failure threshold of degrading systems. Newton 2025;1(3).
[31] Zuo L, Li G, Ding S, Li Z, Zhou H, Bao S, Li B. Predicting fatigue crack growth rate of superalloy GH4169 at high temperature based on thermodynamic entropy generation. Eng Fract Mech 2025;317:110917.
[32] Wei W, Li J, Lin D, Wu F, Yang X. An improved constitutive model for rapid fatigue properties evaluation based on fatigue damage entropy. Eur J Mech A Solids 2025;109:105483.
[33] Han Y, Wu F, Lian Y. Fatigue life prediction of composite laminates based on energy conservation and damage entropy accumulation. Int J Fatigue 2025;199:109088.
[34] Premanand A, Balle F. Heat dissipation and entropy accumulation of CF-PEKK composite under low and ultrasonic frequency loading. Int J Mech Sci 2025;302:110530.
[35] Lee HW, Basaran C. A review of damage, void evolution, and fatigue life prediction models. Metals 2021;11(4):609.
[36] Basaran C. Introduction to unified mechanics theory with applications. Springer Nature; 2023.
[37] Lee HW, Jamal NB, Fakhri H, Ranade R, Egner H, Lipski A, Piotrowski M, Mroziński S, Rao CL, Djukic MB, et al. Unified mechanics of metallic structural materials. In: Comprehensive mechanics of materials, volume 1-4. Elsevier; 2024, p. V3–2.
[38] Basaran C, Lin M, Ye H. A thermodynamic model for electrical current induced damage. Int J Solids Struct 2003;40(26):7315–27.
[39] Li S, Basaran C. A computational damage mechanics model for thermomigration. Mech Mater 2009;41(3):271–8.
[40] Yao W, Basaran C. Computational damage mechanics of electromigration and thermomigration. J Appl Phys 2013;114(10).
[41] Lee HW, Fakhri H, Ranade R, Basaran C, Egner H, Lipski A, Piotrowski M, Mroziński S. Modeling fatigue of pre-corroded body-centered cubic metals with unified mechanics theory. Mater Des 2022;224:111383.
[42] Lee HW, Basaran C. Predicting high cycle fatigue life with unified mechanics theory. Mech Mater 2022;164:104116.
[43] Lee HW, Basaran C, Egner H, Lipski A, Piotrowski M, Mroziński S, Rao CL, et al. Modeling ultrasonic vibration fatigue with unified mechanics theory. Int J Solids Struct 2022;236:111313.
[44] Lee HW, Djukic MB, Basaran C. Modeling fatigue life and hydrogen embrittlement of bcc steel with unified mechanics theory. Int J Hydrog Energy 2023;48(54):20773–803.
[45] Canale G, Lepore M, Bagherifard S, Guagliano M, Maligno A. An experimental validation of unified mechanics theory for predicting stainless steel low and high cycle fatigue damage initiation. Forces Mech 2023;10:100162.
[46] Mangal S, Jamal MNB, Brahmadathan V, Pandey A, Rao CL, Chellapandi P. Micromechanics-based constitutive modelling for creep in nickel-based superalloys using unified mechanics theory. Mater Today Commun 2026;114616.
[47] Michel A, et al. A micromechanical approach to 3D damage modeling in structural steel based on unified mechanics theory. Int J Comput Methods Eng Sci Mech 2026.
[48] Boltzmann L. On the relation between the second law of the mechanical theory of heat and the probability calculus with respect to the theorems on thermal equilibrium. Kais Akad Wiss Wien Math Natumiss Cl 1877;76:373–435.
[49] Planck M. Section 134: Entropie und warscheinlichkeit. In: Vorlesungen uber die theorie der wurmestrahlung. Leipzig, Germany: JA Barth; 1906.
[50] Chebolu LR, Basaran C, et al. Unified mechanics theory based flow stress model for the rate-dependent behavior of bcc metals. Mater Today Commun 2022;31:103707.
[51] Morabito A, Chrysochoos A, Dattoma V, Galietti U. Analysis of heat sources accompanying the fatigue of 2024 T3 aluminium alloys. Int J Fatigue 2007;29(5):977–84.
[52] Mayer H, Schuller R, Fitzka M. Fatigue of 2024-T351 aluminium alloy at different load ratios up to 1010 cycles. Int J Fatigue 2013;57:113–9.
[53] Marti N, Favier V, Gregori F, Saintier N. Correlation of the low and high frequency fatigue responses of pure polycrystalline copper with mechanisms of slip band formation. Mater Sci Eng: A 2020;772:138619.
[54] Sangid MD. The physics of fatigue crack initiation. Int J Fatigue 2013;57:58–72.
[55] Wang X, Feng E, Jiang C. A microplasticity evaluation method in very high cycle fatigue. Int J Fatigue 2017;94:6–15.
[56] Ustrzycka A, Mróz Z, Kowalewski Z, Kucharski S. Analysis of fatigue crack initiation in cyclic microplasticity regime. Int J Fatigue 2020;131:105342.
[57] Jirandehi AP, Khonsari M. On the determination of cyclic plastic strain energy with the provision for microplasticity. Int J Fatigue 2021;142:105966.
[58] Salvati E. Evaluating fatigue onset in metallic materials: Problem, current focus and future perspectives. Int J Fatigue 2024;188:108487.
[59] Mughrabi H. Cyclic slip irreversibilities and the evolution of fatigue damage. Met Mater Trans B 2009;40(4):431–53.
[60] Bach J, Möller J, Göken M, Bitzek E, Höppel H. On the transition from plastic deformation to crack initiation in the high-and very high-cycle fatigue regimes in plain carbon steels. Int J Fatigue 2016;93:281–91.
[61] Polák J, Man J, Vystavěl T, Petrenec M. The shape of extrusions and intrusions and initiation of stage I fatigue cracks. Mater Sci Eng: A 2009;517(1–2):204–11.
[62] Takahashi Y, Yoshitake H, Nakamichi R, Wada T, Takuma M, Shikama T, Noguchi H. Fatigue limit investigation of 6061-T6 aluminum alloy in giga-cycle regime. Mater Sci Eng: A 2014;614:243–9.
[63] McEvily Jr A, Johnston T. The role of cross-slip in brittle fracture and fatigue. Int J Fract Mech 1967;3(1):45–74.
[64] Wagner D, Petit J. Occurrence and evolution of slips markings in a single phase BCC $\alpha$-iron and a low carbon steel during very high cycle fatigue regime. Int J Fatigue 2025;109206.

[65] Lemaitre J, Sermage J, Desmorat R. A two scale damage concept applied to fatigue. Int J Fract 1999;97(1):67–81.
[66] Mahal M, Blanksvärd T, Täljsten B. A two-scale damage model for high-cycle fatigue at the fiber-reinforced polymer–concrete interface. Finite Elem Anal Des 2016;116:12–20.
[67] Wei W, He L, Chen M, Chen X, Liang R, Zou L, Yang X. A two-scale thermodynamic entropy model for rapid high-cycle fatigue property evaluation of welded joints. Eng Fract Mech 2023;292:109614.
[68] Kröner E. Zur plastischen verformung des vielkristalls. Acta Metall 1961;9(2):155–61.
[69] Berveiller M, Zaoui A. An extension of the self-consistent scheme to plastically-flowing polycrystals. J Mech Phys Solids 1978;26(5–6):325–44.
[70] Charkaluk E, Constantinescu A. Dissipative aspects in high cycle fatigue. Mech Mater 2009;41(5):483–94.
[71] Eyring H. Viscosity, plasticity, and diffusion as examples of absolute reaction rates. J Chem Phys 1936;4(4):283–91.
[72] Kula A, Holmedal B, Niewczas M. Plasticity of solid solution Al-Mn and Al-Mn-Si alloys. Mater Sci Eng: A 2024;890:145933.
[73] Lemaitre J, Chaboche J-L. Mechanics of solid materials. Cambridge University Press; 1994.
[74] Voyiadjis GZ, Al-Rub RKA. Thermodynamic based model for the evolution equation of the backstress in cyclic plasticity. Int J Plast 2003;19(12):2121–47.
[75] Srivatsan T. An investigation of the cyclic fatigue and fracture behavior of aluminum alloy 7055. Mater Des 2002;23(2):141–51.
[76] Man J, Petrenec M, Obrtlík K, Polak J. AFM and TEM study of cyclic slip localization in fatigued ferritic X10CrAl24 stainless steel. Acta Mater 2004;52(19):5551–61.
[77] Gregor V, Kratochvil J, Saxlova M. The model of PSB formation. Mater Sci Eng: A 1997;234:209–11.
[78] Buque C. Dislocation structures and cyclic behaviour of [011] and [111]-oriented nickel single crystals. Int J Fatigue 2001;23(8):671–8.
[79] Kubin L, Sauzay M. Persistent slip bands: Similitude and its consequences. Acta Mater 2016;104:295–302.
[80] Hull D, Bacon DJ. Introduction to dislocations, vol. 37, Elsevier; 2011.
[81] Ashraf F, Castelluccio GM. A robust approach to parameterize dislocation glide energy barriers in FCC metals and alloys. J Mater Sci 2021;56(29):16491–509.
[82] Spikes H. Stress-augmented thermal activation: Tribology feels the force. Friction 2018;6(1):1–31.
[83] Taylor G. Thermally-activated deformation of BCC metals and alloys. Prog Mater Sci 1992;36:29–61.
[84] Ventelon L, Willaime F, Clouet E, Rodney D. Ab initio investigation of the Peierls potential of screw dislocations in bcc Fe and W. Acta Mater 2013;61(11):3973–85.
[85] Itakura M, Kaburaki H, Yamaguchi M. First-principles study on the mobility of screw dislocations in bcc iron. Acta Mater 2012;60(9):3698–710.
[86] Testa G, Bonora N, Ruggiero A, Iannitti G. Flow stress of bcc metals over a wide range of temperature and strain rates. Metals 2020;10(1):120.
[87] Eshelby JD. The determination of the elastic field of an ellipsoidal inclusion, and related problems. Proc R Soc Lond Ser A. Math Phys Sci 1957;241(1226):376–96.
[88] Argon A. Strengthening mechanisms in crystal plasticity, vol. 4, OUP Oxford; 2007.
[89] Zhao T, Jiang Y. Fatigue of 7075-T651 aluminum alloy. Int J Fatigue 2008;30(5):834–49.
[90] Peralta P, Laird C. Cyclic plasticity and dislocation structures. In: Reference module in materials science and materials engineering. Amsterdam, The Netherlands: Elsevier; 2016,
[91] Zhang K, Holmedal B, Mánik T, Saai A. Assessment of advanced Taylor models, the Taylor factor and yield-surface exponent for FCC metals. Int J Plast 2019;114:144–60.
[92] Zhu Q, Wang C, Yang K, Chen G, Qin H, Zhang P. Plastic deformation behavior of a nickel-based superalloy on the mesoscopic scale. J Mater Sci Technol 2020;40:146–57.
[93] Karami JS, Sepahi-Boroujeni S, Khodsetan M. Investigating the effects of expansion equal channel angular extrusion (Exp-ECAE) on dynamic behavior of AA7075 aluminum alloy. Int J Adv Des Manuf Technol 2016;9(3).
[94] Wang L, Yang X, Robson JD, Sanders RE, Liu Q. Microstructural evolution of cold-rolled AA7075 sheet during solution treatment. Materials 2020;13(12):2734.
[95] Soares E, Bouchonneau N, Alves E, Alves K, Araújo Filho O, Mesguich D, Chevallier G, Laurent C, Estournès C. Microstructure and mechanical properties of AA7075 aluminum alloy fabricated by spark plasma sintering (SPS). Materials 2021;14(2):430.
[96] Wu P, Song K, Liu F. Effect of coherent nanoprecipitate on strain hardening of Al alloys: breaking through the strength-ductility trade-off. Materials 2024;17(17):4197.
[97] Ryu S, Cai W. Stability of eshelby dislocations in FCC crystalline nanowires. Int J Plast 2016;86:26–36.
[98] Rollett AD, Campman R, Saylor D. Three dimensional microstructures: statistical analysis of second phase particles in AA7075-T651. In: Materials science forum, vol. 519, Trans Tech Publ; 2006, p. 1–10.
[99] Singh SS, Schwartzstein C, Williams JJ, Xiao X, De Carlo F, Chawla N. 3D microstructural characterization and mechanical properties of constituent particles in Al 7075 alloys using X-ray synchrotron tomography and nanoindentation. J Alloys Compd 2014;602:163–74.
[100] Winter A. A model for the fatigue of copper at low plastic strain amplitudes. Phil Mag 1974;30(4):719–38.
[101] Sauzay M, Kubin LP. Scaling laws for dislocation microstructures in monotonic and cyclic deformation of fcc metals. Prog Mater Sci 2011;56(6):725–84.
[102] Agius D, Kajtaz M, Kourousis KI, Wallbrink C, Hu W. Optimising the multiplicative AF model parameters for AA7075 cyclic plasticity and fatigue simulation. Aircr Eng Aerosp Technol 2018;90(2):251–60.